

To appear in The Astrophysical Journal 000, 000000 (2009)

## Mid-Infrared Variability of protostars in IC 1396A

M. Morales-Calderón<sup>1</sup>, J. R. Stauffer<sup>2</sup>, L. Rebull<sup>2</sup>, B. A. Whitney<sup>3</sup>, D. Barrado y Navascués<sup>1</sup>,  
D. R. Ardila<sup>2</sup>, I. Song<sup>4</sup>, T. Y. Brooke<sup>4</sup>, L. Hartmann<sup>5</sup>, and N. Calvet<sup>5</sup>

mariamc@laeff.inta.es

### ABSTRACT

We have used Spitzer/IRAC to conduct a photometric monitoring program of the IC1396A dark globule in order to study the mid-IR (3.6 - 8  $\mu\text{m}$ ) variability of the heavily embedded Young Stellar Objects (YSOs) present in that area. We obtained light curves covering a 14 day timespan with a twice daily cadence for 69 YSOs, and continuous light curves with approximately 12 second cadence over 7 hours for 38 YSOs. Typical accuracies for our relative photometry were 1-2% for the long timespan data and a few mmag, corresponding to less than 0.5%, for the 7 hour continuous “staring-mode” data. More than half of the YSOs showed detectable variability, with amplitudes from  $\sim 0.05$  mag to  $\sim 0.2$  mag. About thirty percent of the YSOs showed quasi-sinusoidal light curve shapes with apparent periods from 5-12 days and light curve amplitudes approximately independent of wavelength over the IRAC bandpasses. We have constructed models which simulate the time dependent spectral energy distributions of Class I and II YSOs in order to attempt to explain these light curves. Based on these models, the apparently periodic light curves are best explained by YSO models where one or two high latitude photospheric spots heat the inner wall of the circumstellar disk, and where we view the disk at fairly large inclination angle. Disk inhomogeneities, such as increasing the height where the accretion funnel flows to the stellar hotspot, enhances the light curve modulations. The other YSOs in our sample show a range of light curve shapes, some of which are probably due to varying accretion rate or disk shadowing events. One star, IC1396A-47, shows a 3.5 hour periodic light curve; this object may be a PMS Delta Scuti star.

*Subject headings:* infrared: stars; stars: pre-main sequence; stars: variables: other

---

<sup>1</sup>Laboratorio de Astrofísica Estelar y Exoplanetas (LAEX), Centro de Astrobiología (CAB, INTA-CSIC). LAEFF, P.O. 78, E-28691, Villanueva de la Canada, Madrid, Spain.

<sup>2</sup>Spitzer Science Center, California Institute of Technology, Pasadena, CA 91125.

<sup>3</sup>Space Science Institute, 4750 Walnut St. Suite 205, Boulder, CO 80301.

<sup>4</sup>Astronomy Department, MC 105-24, California Institute of Technology, Pasadena, CA 91125.

<sup>5</sup>Dept. of Astronomy, University of Michigan, 500 Church Street, Ann Arbor, MI 48109.

## 1. INTRODUCTION

IC1396A (aka "The Elephant Trunk Nebula") is a prominent dark-globule seen projected onto the bright nebular emission of the HII region IC1396. IC1396 is itself part of the larger Cepheus OB2 association, which includes young clusters with ages ranging from 10-12 Myr (NGC 7160), to 4 Myr (Tr 37), to  $< 1$  Myr (the proto-clusters forming in globules such as IC1396A and IC1396N). Reach et al. (2004) reported the first Spitzer observations of IC1396A, where they used IRAC to identify three Class 0 or I protostars and a dozen Class II YSO's within the boundaries of the globule. Sicilia-Aguilar et al. (2006) reported the results of a much wider area Spitzer IRAC and MIPS survey of the Cepheus OB2 association, where they derived disk frequencies and Spectral Energy Distribution (SED) shapes for stars in Tr 37, NGC7160 and in IC1396A. Sicilia-Aguilar et al. identified more than 50 YSO's in IC1396A, including 11 Class I stars and 32 Class II YSO's. They suspected that a number of other YSO's were present in the field of view, but they could not be confirmed either because there was too much nebular contamination of the photometry or because their observations did not allow them to identify Class III sources (YSO's lacking IR excesses).

Most of the IC1396A YSO population is heavily extincted, so there is relatively little literature describing this proto-cluster. Because it is embedded in the IC1396 HII region, the normally assumed distance to the globule is that adopted for IC1396 and Tr 37, which is 900 pc (Contreras et al. 2002). Sicilia-Aguilar et al. compared optical photometry and spectral type data for six of the most lightly reddened globule members to Siess et al. (2000) isochrones, and concluded that these IC1396A stars have an average age of  $\sim 1$  Myr. The more heavily embedded members could presumably be even younger.

We have obtained time-series monitoring of the YSO's in IC1396A using Spitzer's IRAC camera in order to (a) study the temporal variability of these very young, heavily embedded stars and (b) identify additional members of the globule population. In Section 2, we describe the observations and our photometric data analysis. In Section 3, we provide new, deeper maps of the globule based on co-adding all of our observations and from these images construct a new list of YSO members of the globule population. Our time-series photometry and identification of variable stars is described in Sec. 4, while Sec. 5 includes a discussion of the different kinds of variability found and possible physical mechanisms to explain the variability. Finally, we summarize our findings in Sec. 6.

## 2. OBSERVATIONS

The goal of this program was to obtain well-sampled photometry for the protostars in IC1396A on timescales both of hours and days. Several previous programs have demonstrated that IRAC can provide extremely accurate and stable time-series photometry through the detection of the thermal emission of extra-solar planets (Charbonneau et al. 2005; Deming et al. 2007) and the attempt to detect cloud formations in the photospheres of brown dwarfs (Morales-Calderón et al. 2006). Thus

we have used a recent DDT program (PI: Soifer, PID:470) to study mid-IR variability of protostars in the very young star forming globule IC1396A. The data were collected from January 24 to February 6, 2008 and observations were performed with two distinctly different observing modes:

- **Mapping mode:** IRAC imaging was obtained for the whole IC1396A globule in mapping mode. About every 12 hours for 14 days, a short AOR was run to make a 2x3 map with individual exposures of 12 seconds frametime (corresponding to 10.4 second exposure times) and a five position dithering at each map step. The IRAC maps do not cover the same FOV in all bands, providing a region of  $\sim 10 \times 11.5'$ , centered at 21:36:30.85 +57:29:49.37 with photometry in the four IRAC bands (see Figure 1). 52 YSOs from Sicilia-Aguilar et al. (2006) and 13 YSOs from Reach et al. (2004) (11 of which are in common with the sample from Sicilia-Aguilar et al.) are included in this region.
- **Staring mode:** In addition, on February 6, a long staring AOR was performed. This AOR consisted of  $\sim 7.5$  hours of continuous monitoring with no dithering or mapping to get a continuous set of photometry for a  $\sim 5 \times 5'$  region. A total of 2000 single observations, of 12 seconds frametime each, were performed. The Ch. 2 and 4 FOV was positioned at the core of the globule and it included 37 previously known YSOs. The center of the Ch. 1 and Ch. 3 FOV is offset from the Ch. 2 and Ch. 4 FOV by of order  $7'$  to the SE. No previously known YSO's fall in that region. See Figure 1 for further information on the layout of observations.

We will use the staring data (Ch. 2 & Ch. 4) to study the short term (from minutes to hours) variability and the mapping data (all channels) to analyze longer term (up to 14 days) variability. In addition, the mapping observations will be combined to produce new deeper maps and search for new members of the globule.

## 2.1. Mapping Data Photometry

Our starting point for the data analysis was the post-Basic Calibrated Data (postBCD) mosaic image produced by the IRAC pipeline software (ver. S17.0.4). All the data have been analyzed with IRAF standard procedures. We performed aperture photometry using PHOT with a source aperture of 3 pixels radius ( $3.''60$ ). The aperture radius was selected in order to obtain the maximum signal-to-noise ratio. The sky background was subtracted using a 4 pixels ( $4.''80$ ) wide annulus. The corresponding aperture corrections, taken from the *Spitzer* web page have been applied. The mean exposure time for the final mosaics is 52 seconds and we have a total of 28 exposures taken every 12 hours. Calculating appropriate photometric errors is crucial in order to apply variability tests such as the  $\chi^2$  test and thus we decided to compute the photometric errors empirically from the data themselves. Figure 2 plots the observed photometric rms in the time series for each star

detected at 3.6, 4.5, 5.8, and 8.0  $\mu\text{m}$  respectively, as a function of magnitude. We used a polynomial fit close to the lower envelope for each IRAC channel as the estimated photometric uncertainty for a given magnitude.

An example of the time series for one of our non-variable targets can be seen in Figure 3.

## 2.2. Staring Data Photometry

In the case of the Staring data, our starting point was the individual Basic Calibrated Data (BCD) frames produced by the IRAC pipeline software (ver. S17.0.4) at the Spitzer Science Center (SSC). This pipeline produces fully flux-calibrated images, in units of  $\text{MJysr}^{-1}$ , that have had most of the instrumental signatures removed. Some artifacts remain in the pipeline processed data, however - so we have used IDL code provided by the Spitzer Science Center to correct for column pull down and muxbleed (Ch. 1 and 2 features produced by the presence of very bright sources).

As for the mapping data, aperture photometry was performed in each image using PHOT with an aperture of 3 pixels radius, a background annulus of 4 pixels width and the appropriate aperture corrections<sup>1</sup>. In order to improve the signal-to-noise ratio, the BCD images were combined in groups of 5. Therefore, we have 400 merged data points with 1 minute increments spanning almost 7.5 hr of observation time.

Figure 4 illustrates the pointing stability during these observations. Only a very small (less than 0.3") periodic movement is seen. This effect is systematic and documented in the *Spitzer* web page. Such motion can affect the Ch. 2 fluxes at of order the 1% level; however, because we know the pointing movements precisely, we can identify any photometric variations related to this effect. Because we see no measureable variations on the timescale of the pointing drift, we have not attempted to correct our photometry for the “pixel-phase” effects. The uncertainties in the light curves were computed empirically. We assumed that no significant real variability in our objects occurs on timescales of 10 minutes or less. We measured the scatter of every 10 data points, and the  $1\sigma$  error bars in the figures represent the median of these values.

The brightest objects of our sample show an upward trend in brightness of  $<3\%$  from the beginning to the end of the observation at Ch. 4. Because the same trend cannot be seen in the Ch. 2 data and because this variation only appears in the brightest objects, we believe that it is due to the latent image charge buildup, an instrumental effect that was also observed in previous cases with similar kinds of data (Charbonneau et al. 2005; Morales-Calderón et al. 2006). This instrumental effect may depend on the flux of the target and there is also a pixel-dependent term in the behavior of the long-term latents. In addition, it is possible that they are frame time

---

<sup>1</sup>The BCD data have the native pixel scale of about  $1.22''/\text{pixel}$  and have not been distortion corrected, so the standard aperture correction is only approximately correct; however, since our interest is only in photometric variability the small errors this introduces are irrelevant.

dependent. To derive a first-order correction for this effect, we have selected a bright, non-variable star in our data and fitted a second-order polynomial to its normalized flux. We approximately correct the fluxes for all other bright stars (approx.  $[8.0]<10$ ) which show this trend, by dividing their time series photometry by this polynomial fit.

### 3. COMBINED MAPS

In addition to the individual mosaics, we have co-added all the mapping mode observations using MOPEX in order to produce a new deeper map. The photometry has been obtained in the same way as in the previous cases and we have used the IRAC color-color diagram,  $[3.6]$ - $[4.5]$  vs.  $[5.8]$ - $[8.0]$ , to target possible candidates and analyze their time series too. Thus, we are requiring our new candidate members to have detections at all IRAC bands. This color-color diagram was presented as a tool to separate young stars of different classes (Allen et al. 2004; Megeath et al. 2004), depending on where they fall in the diagram. Note however that Class III objects cannot be separated from field objects due to their lack of infrared excess. The Elephant Trunk Nebula is embedded in a web of bright, spatially variable nebulosity which is brightest at  $8 \mu\text{m}$  while normal stars are usually faint at that wavelength. Thus, we have excluded from our list of new candidates those objects showing large  $[5.8]$ - $[8.0]$  but small  $[3.6]$ - $[4.5]$  colors, and that are located within the brightest parts of the nebulosity or the parts with largest gradients between wavelengths. In addition, we have eliminated from our list all the objects with errors larger than 0.1 mag in one or both of the bluer IRAC bands in order to have a reliable sample of new candidate members. Figure 5 shows the IRAC  $[3.6]$ - $[4.5]$  vs.  $[5.8]$ - $[8.0]$  diagram with the previously known YSOs as well as our new candidates plotted.

In addition, we have used the spectral energy distribution (SED) of each source as a way to characterize the structure of its circumstellar disk. After Lada et al. (2006) we have used the 3.6-8.0  $\mu\text{m}$  slope for each source detected in all four IRAC bands to distinguish between objects with optically thick, primordial disks ( $\alpha_{IRAC} > -1.8$ ), objects surrounded by optically thin or anemic disks ( $-2.56 < \alpha_{IRAC} < -1.8$ ) and objects without disks ( $\alpha_{IRAC} < -2.56$ ). This is based on the distribution of the disk population in Taurus (1-2 Myr). The SEDs of our new targets can be seen in Figure 6. We have used previous observations from the Spitzer archive to derive the fluxes of our new targets at 24  $\mu\text{m}$  (PID:58, PI:Rieke). Most of our new candidates are located within the head of the globule, where the emission at 24  $\mu\text{m}$  is very intense and thus we were able to derive magnitudes for only a few of our targets. Our new candidate members with their photometry and assigned evolutionary class (by means of the IRAC color-color diagram) are provided in Table 1. All these objects have thick disks based on their IRAC SED slope.

#### 4. TIME SERIES AND PRESENCE OF VARIABILITY

We have tabulated and examined the time series photometry for all of the objects detected in the mapping and staring data.  $1\sigma$  rms uncertainties of  $\sim 2$  mmag in Ch. 2 and  $\sim 4$  mmag in Ch. 4 for the brightest targets are achieved for the staring data. For the mapping data the lowest uncertainties achieved are of order 6 mmag in the two bluest bandpasses. The light curves of all previously known and new candidate members were visually inspected. In this way different types of variability, that may be difficult to pick out in an automated fashion, can be spotted while bad photometric measurements can be eliminated. However, this process is totally subjective. Since we wanted to search for variability also in the field, and given the large number of detections, we have used the  $\chi^2$  test and the Stetson J statistic as quantitative estimators of photometric variability for both short- and long-term variability.

The  $\chi^2$  test determines the probability that the deviations in a light curve are consistent with the photometric errors (i.e., nonvariable). The null hypothesis for the test is that there is no variability. We evaluated the  $\chi^2$  statistic,

$$\chi^2 = \sum_{k=1}^{k=K} \left( \frac{\Delta m(k)}{\sigma} \right)^2 \quad (1)$$

where  $K$  is the number of data points in the light curve,  $\Delta m(k)$  is the magnitude for each data point with the mean magnitude subtracted, and  $\sigma$  is the rms error in the photometry. A large  $\chi^2$  value indicates a greater deviation compared to the photometric errors and thus a smaller probability that the null hypothesis is true (i.e., variable). This probability,  $p$ , is calculated, and we claim evidence for variability if  $p < 0.01$ . Because this method is very sensitive to the accuracy of the error estimation, our technique of using the data to empirically estimate the errors should minimize false detections. In addition, since a single bad measurement can produce high  $\chi^2$  values, we eliminated from the time series the  $3\sigma$  isolated deviants prior to calculating the statistic.

The  $\chi^2$  test does not take advantage of correlated changes in multiband time series and thus we used the Stetson variability index,  $J$ , (Stetson 1996) to try to identify low amplitude, correlated variables. The Stetson variability index was computed for each star from the four IRAC bands magnitudes and their associated photometric uncertainties as

$$J = \frac{\sum_{k=1}^n w_k \text{sgn}(P_k) \sqrt{|P_k|}}{\sum_{k=1}^n w_k} \quad (2)$$

where we assign, to each of the  $n$  pairs of observations considered, a weight  $w_k$ , and

$$P_k = \begin{cases} \delta_{i(k)} \delta_{j(k)} & \text{if } i(k) \neq j(k) \\ \delta_{i(k)}^2 - 1 & \text{if } i(k) = j(k) \end{cases} \quad (3)$$

is the product of the normalized residuals of the two paired observations  $i$  and  $j$ , and

$$\delta_i = \sqrt{\frac{n}{n-1}} \frac{m_i - \bar{m}}{\sigma_i} \quad (4)$$

is the magnitude residual of a given observation from the average normalized by the standard error. For a non variable star, with only random noise, the Stetson variability index should be scattered around zero and have higher, positive values for stars with correlated physical variability. Figure 7 shows the Stetson statistic as a function of the [3.6] magnitude. The dashed line at  $J = 0$  shows the expected value of the variability index for non variable stars, and the dotted line at  $J=0.55$  represents the minimum value adopted by Carpenter et al. (2001) in a similar near-IR variability study toward a several square degree area in the Orion. Most of our targets have magnitudes brighter than  $[3.6]=13.5$  and only one (catalogued by both the  $\chi^2$  test and the J statistic as non variable) has a magnitude fainter than  $[3.6]=14.2$ . Following the choice adopted by Carpenter et al. (2001), and based on our own comparison of the  $\chi^2$  and J statistic results for individual stars, we adopt  $J = 0.55$  as the borderline between variable and non variable objects. However, we note that the J index shows higher dispersion towards fainter magnitudes and a different minimum value should be used for fainter objects.

If evidence of variability was found in an object, we looked for a periodic signal in the data following the methodology described by Scargle (1982). This method is equivalent to a least squares fit (in the time domain) of sinusoids to the data. The algorithm calculates the normalized Lomb periodogram for the data and gives us a false-alarm probability based on the peak height in the periodogram as a measure of significance. There is, in general a good agreement between the periods found at different wavelengths, however caution should be taken since in most cases our data only cover a time frame of order the estimated period.

## 5. RESULTS AND DISCUSSION

### 5.1. The mapping data: long-term variable members

Fifty two previously known YSOs from Sicilia-Aguilar et al. (2006) and 13 YSOs from Reach et al. (2004) (11 of them are in common with the sample from Sicilia-Aguilar et al. (2006)) plus 15 new candidates fall inside the area of our mosaics, and most of them have good photometry in the four IRAC bands. As the first step to determine their variability, we applied the  $\chi^2$  test to the Ch. 1 & Ch. 2 data. We did not calculate  $\chi^2$  for the longer wavelength channels because those data are much noisier. Forty stars were labeled by the  $\chi^2$  statistics as variable objects in IRAC Ch. 1 and Ch. 2 while 4 objects, IC1396A-62, IC1396A-63, IC1396A-66, and IC1396A-72, were found to be variable only in Ch. 1. Two of these objects, IC1396A-62 and IC1396A-63 are located near the border of the Ch. 2 & Ch. 4 mosaics and are outside the FOV in most of them; however, the light curve built for these objects with the photometry of Ch. 3 confirms the variation shown in Ch. 1. IC1396A-66 shows low amplitude variations in Ch. 1 but the light curves at longer wavelengths, even when they follow the same trend, are too noisy to confirm the variation. Object 72 has been detected in the deep mosaics which have been built combining all the individual maps, however in the individual observations only the Ch. 1 data is good enough to build its time series. We thus

cannot confirm the Ch. 1 result, and consider object 72 non-variable.

As the other primary means to determine variability, we also calculated the Stetson J variability index using the four IRAC bands for each source. 12 objects labeled as variable by the  $\chi^2$  test were labeled as non variable by the J index however, all but three of them (objects 19, 30, and 51) are labeled as variable if one excludes Ch. 4 to calculate the J statistic. We have given a final tag – variable (V) or non variable (N)– to each source based on the  $\chi^2$  test, the J index, and a careful visual inspection of all the light curves. The very good similarity, in most cases, between the light curve shape for Ch. 1 and for Ch. 2 (and 3 and 4 when the S/N is good enough) is good evidence that the variability is real. Only one star showed what we believe is real variability in Ch. 3 or 4 but not in the shorter wavelength channels. That object is IC1396A-74 (see later discussion and Figure 11b).

Table 2 presents the results of all targets including IRAC magnitudes, rms amplitudes, result of the  $\chi^2$  test, J statistic, our final variability tag, and periods for Ch. 1 & Ch. 2. Note the use of the term  $T_{var}$  instead of rotation period in the table indicating that these are variability timescales rather than periods since the timespan of our observations are not long enough to confirm the periodicity. Objects are named following the order in Table 6 of Sicilia-Aguilar et al. (2006) until number 57. Objects 58 and 59 are YSOs from Reach et al. (2004) not in common with Sicilia-Aguilar et al. (2006), and objects from 60 to 74 are our 15 new candidates. YSO classifications for each object derived from the IRAC color-color diagram, are also included as well as the YSO classification previously given for these objects. There are 8 objects marked as having different classification from that in Sicilia-Aguilar et al. (2006). Four of these as Class I by one of us, and Class II by the other, but are really very close to the boundary between those classes. Actually two of those objects (1 and 40) are in common with Reach et al. (2004) where they were classified as Class I/II. The remaining 4 objects were classified by us as Class III because of the lack of IR excess. One of them (-30, previously known as LKHa 349a) was also studied by Reach et al. (2004) and classified as Class III. The remaining 3 objects could be field stars (two of them, 9 and 32 were classified by Sicilia-Aguilar et al. (2006) as possible non members).

There is a range of shapes found in the light curves and Figures 8-12 present the different observed mid-infrared variability characteristics. All variable stars have their photometry tabulated in Table 3, available in the electronic version of this article. About 30% of our YSO's show light curves that resemble the optical variations of BY Dra variables (spotted stars whose apparent luminosities vary due to rotational modulation – Byrne et al. (1987)). T Tauri stars also show such variability in the optical and near-IR, generally attributed to either cool, solar-type spots or hot spots associated with accretion flows onto the stellar photosphere (Rydgren & Vrba 1983; Bouvier et al. 1986; Vrba et al. 1986). It is not obvious, however, whether our mid-IR light curves can be attributed to such spots (see discussion in Sec. 6). Figure 8 shows these periodic-like light curves, where the characteristic timescale of variability increases from the upper left panel to the lower right one. The peak-to-peak variability amplitudes of these objects can be found in Table 4. These data illustrate that the variability amplitudes are essentially invariant with wavelength from



3.6 to 8  $\mu\text{m}$ .

Other types of variability exhibited by one or more of our YSO's include:

- rapid (timescales of hours) variability inconsistent with rotational modulation. No apparent color dependence during the variations. Only two objects present this kind of variations: IC1396A-39 (object  $\eta$  in Reach et al. (2004)) and IC1396A-62 – see Figure 9. Objects 39 and 62 are Class I and Class II, respectively. Possible causes: flares or accretion flickering;
- slow (timescales of days), non-periodic variability changes, with little or no color changes. 20% of our sample of YSOs fall under this category. Their light curves are shown in Figure 10. Only three Class I YSOs (IC1396A-1, IC1396A-8, and IC1396A-50) are included in this group. Possible causes: accretion variations; rapidly evolving spots. We admit there is in some cases ambiguity whether an object should be in Fig 8 or 10 - the time span of our observations is too short for certainty.
- slow (timescales of days), flux modulation with color dependence. Three objects of our sample show this kind of variations: IC1396A-57 (Figure 11a), which shows a slow brightening over the entire 14 days of observation with a slower rise to maximum going to longer wavelengths, and IC1396A-35 (Object  $\beta$  in Reach et al. (2004) –Figure 12), which shows a slow fading over about five days, followed by a sudden reset to the original brightness and then approximately constant flux at 3.6 and 4.5 microns for the remaining time. IC1396A-35 is the only YSO with significant, coherent color variation over the 14 day observing run - becoming significantly redder when faint. Another possible exemplar of this class is IC1396A-74, which shows essentially constant magnitude at 3.6, 4.5 and 5.8 microns, but an apparently significant decrease in flux over a several day period at 8 microns (Figure 11b). Objects 35 and 57 are Class II stars and object 74 is a Class I YSO. Possible causes: radially differential heating of the inner disk; obscuration by an inner disk over-density.

## 5.2. The staring data: short-term variable members.

Thirty eight out of the 42 targets that fall inside the FOV of Ch. 2 & Ch. 4 in the staring mode observations have enough good photometry to derive their time series, at least in one of the two band passes. The remaining objects were saturated in our images (IC1396A-19 and IC1396A-30) or were too faint to obtain their photometry (IC1396A-26 and IC1396A-27). Five out of these 38 objects are new candidate members based on our new deep photometry. Table 5 presents the results of all targets including IRAC magnitudes, rms amplitudes for the light curves, result of the  $\chi^2$  test, the period of the modulation observed if there is any, the J variability index, and our final tag of variability. 14 objects were labeled by the  $\chi^2$  statistic as variable in Ch. 2, however only 4 of them were labeled as variable in both band passes, IC1396A-35, IC1396A-47, IC1396A-57, and IC1396A-61 (Figure 13 shows the light curves of the short-term variable stars). Another 7 objects

where labeled as variable by the J variability index. The most interesting object is IC1396A-47, which shows a period of 3.4 hr in both band passes (we discuss this star in more detail in Sec. 6.4). A few of the objects labeled as variable in Ch. 2, but not in Ch. 4 by the  $\chi^2$  test, have light curves in Ch. 4 which follow the same trend and have similar amplitude to that of the light curve in Ch. 2. They have not been labeled as variable at Ch. 4, probably due to a much higher noise at 8.0  $\mu\text{m}$  than at 4.5  $\mu\text{m}$ . These objects are IC1396A-22, IC1396A-24, IC1396A-39, and IC1396A-43 – two of them are variable based on the J index and the other two are just below the adopted J index limit for variable stars. We consider the four of them as variable objects due to the shape similarity between both bandpasses. The remaining objects show amplitudes in Ch. 2 of order of the noise seen in the light curves in Ch. 4, not allowing the detection of variability in the latter channel. There is only one object, IC1396A-25, which has detected variability based on the  $\chi^2$  test only in Ch. 4. This object is variable based on the J index however, it is very bright at 8  $\mu\text{m}$  and since latent build-up seems to be flux dependent, it is possible that our correction is not good enough for this object and the variability is instead spurious. The four objects with detected variability in both bandpasses show the same light curve shape in each band, IC1396A-35 and IC1326A-61 show a downward trend during the 7.5 hr of observation, and IC1396A-47 presents a pulsation like variation (see Sec. 6.4). The last object labeled as variable in both channels, IC1396A-57, shows  $\chi^2$  values that are only slightly above our detection threshold. Its light curves show a low amplitude correlated variation and it is labeled as variable by the J index. IC1396A-57 does vary on long timescales, as shown in Figure 11. Finally there are two objects which lack good photometry in Ch. 4 –IC1396A-54 and IC1396A-60– but which show an upward trend in their Ch. 2 light curves. Since we cannot confirm the variability with the Ch. 4 data we do not include those objects in the final list of variable YSOs. Their light curves can be seen in Figure 14.

To summarize, 8 out of 38 YSOs show correlated short-term variability in Ch. 2 and Ch. 4. All these objects also show long-term variability (see Sec. 5.1) and the variations seen in the 7.5 hr period are consistent with the light curve shapes seen in the mapping mode data (note that the staring observations were performed 5 hr after the last mapping observation was finished).

The remaining objects are catalogued as non-variable in short-timescales and any possible variability has to be under the rms amplitudes quoted in Table 5.

### 5.3. Variability of stars without IR excesses in the mapping data

In addition to the previously known members we have inspected the “field” (which includes both true field stars and YSO’s lacking IR excesses) stars, in search of additional variable stars. Due to their lack of infrared excess, Class III YSO’s cannot be separated from field objects at *Spitzer* wavelengths. However, given that photometric variability is one of the original defining characteristics of pre-main sequence stars, the detection of variability can be used as a possible indicator of youth. Thus, we applied the  $\chi^2$  and J statistics to the entire sample of detected objects in Ch. 1 and Ch. 2. 6% of the sample was labeled as variable in both tests. We visually inspected

the light curves of all these objects to remove spurious variability detections due to bad photometric measurements or very noisy light curves. We identify 46 objects as being variable both in the visual inspection and in the statistical tests. Most of the light curves of these objects are consistent with rotational modulation with periods of order 4- >10 days. These objects present Rayleigh-Jeans-like SEDs with no infrared excess other than contamination expected from the nebulosity. While we are reasonably convinced these stars are variable at 3.6 and 4.5 microns, without further data we cannot know whether they are members of IC1396A, members of the older Tr37 cluster, spotted field stars, or other variables of uncertain type. Data at other wavelengths are needed to categorize these stars. Light curves for a few of these new candidates can be seen in Figure 15 and their photometry is presented in Table 6.

#### 5.4. Properties of the variable YSOs

As summarized in Table 7, 41 out of the 69 objects that form our sample of YSOs (54 previously known YSOs plus 15 new candidates) are variable on long timescales. Forty percent of the 69 YSOs in Table 2 show peak-to-peak amplitudes of at least 0.1 mag and 60% of the sample present peak-to-peak amplitudes greater than 0.05 mag. Most of the variable YSOs show colorless variations (at least within the photometric errors) but there are 3 objects whose IRAC colors vary with time. In two out of them the object gets redder as it gets fainter, as would be expected if variable extinction or rotational modulation of a spotted photosphere is the cause of the photometric changes. 23 YSOs show what seems to be well-defined apparently periodic variability with amplitudes up to about 0.2 mag. Where we are able to derive estimated periods, the periods range from about 5 days to about 11 days. These variables include 9 Class I and 14 Class II objects.

In order to help determine the physical cause(s) for this variability, it is useful to determine if there is anything special about the variable stars - i.e. are they younger than average? are they more embedded than average? are they higher or lower mass than average? Figure 16 shows the spatial distribution of the different types of YSO's. The figure illustrates that all the Class I and most of the objects with periodic-like light curves are located within the most embedded areas of the nebulosity while the Class II stars seem to be more spread out across the mosaic. Figure 17 shows the IRAC [3.6]-[4.5] vs. [5.8]-[8.0] diagram where the YSOs of different types have been identified (red open diamonds represent large amplitude variables –peak-to-peak amplitudes of at least 0.1 mag– while blue open circles stand for constant objects). The diagram shows that the large amplitude variables tend to be redder in the IRAC colors (though some other stars are also quite red and do not show significant variability with IRAC). We conclude from Figures 16 and 17 that while our large amplitude variables can be either Class I or II, there is a preference for the large amplitude variables to be amongst the evolutionarily youngest stars in our sample. In addition, if we compare the whole sample of YSOs with the group of objects showing periodic-like variations the magnitude distributions are very similar and there is no evidence that the latter ones are more or less massive than the whole sample.

Carpenter et al. (2001) presented a near-IR variability study toward a several square degree area in the Orion A molecular cloud. They found more than a thousand variable stars with a high diversity of photometric behavior. As in our case, most of their variable objects did not show color variations and 18% of them were periodic. They concluded that most of the periodic stars were better explained by cool spot models, primarily because of the small change in color during the variability cycle. Most of the periodic stars were compatible with being WTTs, based on their colors. However, some aspects of the JHK data seemed incompatible with either cool or hot spot models. The small number of objects in our sample, the difference in the sample construction (in particular, the lack of Class III sources in our sample), and the different wavelength coverages prevents us from making any direct statistical comparison with the Carpenter et al. data. In addition, the thermal emission from dust at IRAC wavelengths adds a significant complication which makes it more difficult for the simplest spot models to fit our data, as we discuss in the next section.

## 6. Causes of variability

### 6.1. Accretion variation

We have investigated the possibility that the variation seen in some of our light curves come from changes in the disk mass accretion rate. D’Alessio et al. (2005) have constructed a database of accretion disks models. Using these models we have computed the amplitudes of the variability due to changes of one order of magnitude in the mass accretion rates, from  $10^{-9} M_{\odot}/\text{yr}$  to  $10^{-8} M_{\odot}/\text{yr}$  and from  $10^{-8} M_{\odot}/\text{yr}$  up to  $10^{-7} M_{\odot}/\text{yr}$ . Figure 18 shows the predicted brightness variations computed for two different variations in the accretion rates and two different inclination angles. According to these models, one order of magnitude change in an accretion rate  $\sim 10^{-9} M_{\odot}/\text{yr}$  could produce the amplitudes we see in our light curves particularly if the underlying star is relatively late spectral type. At least for some parameter ranges, the models also predict relatively little variation in IRAC color as a result of the change in accretion rate, as necessary to match most of our variable objects. This mechanism can be causing the non-periodic variability changes on multi-day to week timescales seen in some of our variable YSOs. However, we believe that it is not the predominant mechanism; such rapid, extreme accretion variability would be easily detected at shorter wavelengths, yet few examples have been reported.

### 6.2. Starspots

More than half of the IC1396A variable YSOs have light curves that appear periodic, as shown in Fig 8, with amplitudes 0.1-0.2 mag (See Table 4), and typical periods in the range 5 to more than 11 days. For T Tauri stars observed in the optical or near-IR such variability is thought to originate mainly from either cool magnetic spots (dynamo driven activity) or hot accretion spots on the stellar surface (where the material from the disk falls onto the star) that are hundreds

to thousands of kelvins different in temperature from the photosphere and rotate with the star. Light curve amplitudes in the optical of order 0.2 mag (or considerably larger) are not atypical for CTTs or WTTs. We have contemplated the possibility that hot or cool spots on the photospheres of these YSOs could produce the light curves we observe; using somewhat extreme parameters, light curve amplitudes of order 0.2 mag can be obtained even at IRAC wavelengths. We have estimated the photometric amplitudes expected from both cool and hot star spots using a simple model (Vrba et al. 1986) which assumes that the stellar surface has a spotted region characterized by a single temperature blackbody and is confined to one hemisphere. The amplitude of the light variations as a function of wavelength can be expressed as:

$$m(\lambda) = -2.5 \log\{1 - f[1 - B_\lambda(T_{spot})/B_\lambda(T_*)]\} \quad (5)$$

where  $T_{spot}$  and  $T_*$  are the temperatures of the spot and the photosphere,  $f$  is the maximum fraction of the stellar photosphere covered by spots and  $B_\lambda(T)$  is the Planck function. Note that this star spot model is an approximation since it ignores limb darkening, inclination effects, and opacity differences.

Figure 19 shows the maximum predicted amplitudes at 3.6  $\mu\text{m}$  and color [3.6]-[4.5] for typical stars with temperatures ranging between 3000 K and 6000 K (expected temperatures for 2MASS J magnitudes between 9.5 and 14 mag at 900 pc if one assumes an age of 0.5 Myr (Siess et al. 2000)). We assumed that hot spots (filled circles) have temperatures of order 10000 K, and cold spots (represented by asterisks) have temperatures 1500 K cooler than the photosphere. Different coverage fractions with a maximum of 10% for hot spots, and up to 30% for cold spots are shown. In Figure 20 the maximum amplitude of variation for each channel is shown. These diagrams show that the difference in amplitude between different bandpasses is very small, as is true for our light curves, and the amplitudes are smaller for higher photospheric temperatures.

However, these simple spot models are missing an important contribution relevant to our case. Essentially all of our objects are Class I and Class II YSO's, with significant flux excesses over photospheric at IRAC wavelengths. The Vrba et al. (1986) model assumes all of the flux is coming from photosphere and spots. If warm dust in the disk or envelope contribute substantially to the integrated fluxes at 3.6  $\mu\text{m}$  onward, and if the disk/envelope flux is invariant with time, then the variability amplitudes we observe with IRAC would be substantially lower than predicted by equation 2.

We consider two extreme cases. At one extreme, we consider the case where nearly all of the light we see from the variable YSO's is scattered light. The apparent excess fluxes at IRAC wavelengths are therefore instead indicative of lower extinction to the scattering surface at longer wavelengths, rather than thermal emission from dust in the inner disk/envelope. Since all of the light we see originates from the star, the IRAC light curve amplitudes could be nearly as large as the model estimates, dependent on the geometry assumed for the scattering surface(s). Wood & Whitney have constructed models of Class I YSOs with hot spots illuminating a disk+envelope, and have

shown that even when the direct light from the star is heavily attenuated, the photometric signature of the hot spot (as it rotates with the stellar photosphere) can be seen in the scattered light flux from the envelope, at least at I band. For a model where the star+hot spot had an I band light curve amplitude of around 1 mag and where direct light from the star was almost completely blocked by the disk ( $i = 82$  deg), the scattered light at I band showed a light curve amplitude of about 0.2 mag. A possible prototype for our IC1396A variable objects is HL Tau, where it is believed that essentially all the flux we see at least out to  $2 \mu\text{m}$  is scattered light. If scattered light dominates out to  $8 \mu\text{m}$ , then perhaps the Wood & Whitney model could provide the correct physical model to explain our light curves. With these assumptions, the observed flux at IRAC Ch. 4 provides a lower limit to the photospheric flux of the star at  $8 \mu\text{m}$ . For our stars with quasi-sinusoidal light curves, and assuming an age of 0.5 Myr from Siess 2000, this suggests masses of order 0.3 to  $4.5 M_{\odot}$ , and spectral types of M5 to F3 with the majority of the objects having masses around  $3.5 M_{\odot}$  and spectral types  $\sim\text{K3}$ .

However, it is not obvious that the variable YSOs in IC1396A are as evolutionarily young as HL Tau. Some of them fall in the IRAC color-color diagram within the Class II region, and do not necessarily have any significant remaining infalling envelope to serve as the scattering surface<sup>2</sup>. Also, it is difficult to understand how these stars could have such extreme hot spots (much larger covering factor than typically required to explain CTT light curves in the optical or near-IR) and hence presumably very active accretion without having a significant amount of warm dust contributing strongly to the flux at IRAC wavelengths. Therefore, as the other extreme model, we consider a case where the observed J band magnitude is assumed to provide a reasonable estimate for the photospheric flux of the YSO (an assumption often used when attempting to place YSO's in HR diagrams to estimate their ages). The fluxes at IRAC wavelengths are then the sum of a photospheric component (estimated by taking the J band flux and extrapolating to longer wavelengths with a black-body function) plus excess emission from warm dust. The fraction of the IRAC flux that is emitted by the star then places constraints on models to explain the light curve amplitudes. As an example, we derive  $F_{phot} = 0.09, 0.04, 0.02,$  and  $0.01$  for IRAC Ch. 1 through Ch. 4 for object IC1396A-47 (See Fig. 23), where  $F_{phot}$  is the fraction of the total system flux coming from the star in each of the IRAC bands. In the absence of any other mechanisms, and assuming the disk emission is invariant with time, if the star had an amplitude in its IRAC light curves of 1 mag, the star+disk would have amplitudes of only of order 0.09 mag in Ch1 and 0.01 mag in Ch4. Because no plausible spot model produces light curve amplitudes anywhere near 1 mag at IRAC wavelengths (for just the star alone), and because we see no wavelength dependent variation in amplitude for objects similar to IC1396A-47, we conclude that this simplest star+spot plus disk model cannot account for our observed light curves.

---

<sup>2</sup>We note, however, that according to the models of Robitaille et al. (2007), some Class I YSO's have colors that fall in the Class II region of the IRAC CCD, and therefore it is possible that all of our "periodic" variables may be Class I's.

### 6.3. Variable heating of the disk and disk inhomogeneities

Time varying heating of the inner disk by the rotating spot could provide the mechanism for IRAC variability, if some property of the viewing geometry allows our view of the warmer part of the disk to vary with time. In this case, it is the luminosity of the spot compared to the luminosity of the rest of the photosphere that matters, so if the temperature of the hot spot is twice that of the photosphere, a spot covering fraction of only a little more than 1% could yield a 0.2 mag light curve amplitude from the disk. For this flavor of models, and assuming a medium  $A_v$  of 8 magnitudes, the J band fluxes correspond to a mass range of 0.2 to 1.3 solar mass for our periodic YSO's.

We have constructed models of a Class I protostar (with a disk and envelope, and a photosphere with a hot spot) using the radiative transfer code described in Whitney et al. (2003b,a), and have varied the inputs to these models, including the inclination angle at which we view the disk. If there are hot spots in the photosphere of the object, the disk will be asymmetrically heated too, and that could help keep the variations at IRAC bands at a higher level than if the disk emission were a constant source of additional flux. Figure 21 shows the results of these models for two viewing angles, with the temporal variation of the spectral energy distribution in the left panels, and the magnitude variations in specific bands for one full rotation period of the star in the right panels (asterisk: V-band, diamond: R-band, triangle: [3.6], box: [4.5], open circle: [5.8], and filled circle: [8.0]). A star of mass  $1.5 M_{\odot}$  with effective temperature  $\sim 4300\text{K}$  was used. For accretion parameters, we used a disk mass of  $0.05 M_{\odot}$ , a disk accretion rate of  $8.6 \cdot 10^{-7} M_{\odot}/\text{yr}$ , and an envelope accretion rate of  $4 \cdot 10^{-6} M_{\odot}/\text{yr}$ . A hot spot with a fractional area coverage of 0.3% and a temperature of  $10000\text{K}$  sitting at latitude 45 degrees was added to the models. The figure shows that these models can easily reproduce the IRAC light curves with the right amplitudes with very modest hot spot sizes.

Close examination of the details of the model show that the IRAC variations arise from the heating of the inner disk wall (that is, the IRAC light curves are brightest when the photospheric hot spot is on the far side of the star, heating up the back wall). The IRAC variations are largest at close-to-edge-on viewing angles where the far side of the wall is in view. At more pole-on inclinations (bottom panels of figure 21), the flux from the inner disk shows less phase dependence of our view of the hotter part of the inner disk so contribute less to the overall flux which consequently shows smaller variations. In the optical, the star is brightest when the hot spot is facing the observer. Therefore, the optical and IRAC light curves are 180 degrees out of phase.

Similar results are obtained for a Class II source as shown in Figure 22. The top-left panel shows the same stellar, disk, and hotspot parameters as in Figure 21 but with no envelope. The IRAC variations are similar (the y-axis scales are different), but the visible light curve shows much larger variation in the Class II source. In the Class I source, the visible light is scattered in the envelope, which decreases and washes out the variations. In the Class II source, we clearly see the stellar hotspot rotate out of view and then stay at the same brightness until it rotates into view.

The top right panel of Figure 22 adds a warp to the disk: at the same longitude as the stellar hotspot, the disk height increases by 25% over the nominal value (we use a  $\sin^{11}(\Lambda)$  function, where  $\Lambda$  is the longitude, to make a smooth transition). The warp decays exponentially with radius, with an e-folding distance equal to the inner disk radius  $R_{in}$ ; thus, at a radius of several  $R_{in}$ , the disk becomes axisymmetric. The warp is meant to simulate the effect of an accretion flow to the stellar hotspot, and dragging some dust with it, effectively increasing the height of the disk. A model of this type has previously been proposed to explain the observed optical variability of AA Tau (Bouvier et al. 1997, 2003).

The result of this is that the IRAC variations are larger except at 8  $\mu\text{m}$ . This is because the regions of the wall that is heated by the stellar hotspot has a bigger area than the model with no warp. The optical variations are lower with the inclusion of the warp. This is because the reflection off the warped wall adds flux back into the beam as the hotspot moves out of view.

The bottom panels of Figure 22 show two stellar hotspots separated in longitude by  $180^\circ$ , with one at  $+45^\circ$  latitude and the other at  $-45^\circ$ , and disk warps at these longitudes (one in the  $+z$  direction and the other in the  $-z$ ). These are shown for two different viewing angles (bottom left and right panels). The IRAC light curves are now double peaked due to the two warps. The IRAC variations are similar in the two viewing angles shown (bottom left and right panels), while the visible light curves show large differences. The optical light curves are more complicated due to the geometry of the stellar hotspots, and scattering and obscuration from the warped wall.

These models demonstrate that both hotspots and disk inhomogeneities can explain the variability in the 30% of our sample of YSOs that shows 5-12 day periodic light curves. The amplitudes and behaviors are a function of the spot temperature and size, number of hotspots, viewing angle, and possibly inner disk radius (the latter has not been investigated yet). Multiwavelength observations combined with models should be able to distinguish between single- and double-hotspot models and viewing angles.

#### 6.4. IC1396A-47: Pulsating pre-main sequence star?

Our object IC1396A-47 was previously identified in Reach et al. (2004) as object  $\zeta$ . It has been classified by us and others as a Class I YSO based on its IRAC SED shape and position in the IRAC CCD. However, when we fit its SED using an evolutionary sequence of models from Class 0 to Class III (Whitney et al. 2003b,a), object 47 is best fit with a pure disk model seen nearly edge on, with essentially no envelope, and with a large extinction to explain the very red J-K color. The primary reason why an edge-on Class II model is favored is the low 24  $\mu\text{m}$  flux.

IC1396A-47 shows a periodic variation with a peak-to-peak amplitude of 0.2 mag and a derived period of 9 days in the mapping data (See Fig. 23b). However, this object was the only one also showing a periodic short term variation. As shown in Fig 23a, it exhibits an apparent  $\sim 3.5$  hr periodicity with amplitude of order 0.04 mag. Contact binaries can have similar periods and light



curve shapes; however, for the mass and radius required for object zeta, the apparent period is too short. We believe that the most plausible explanation for the short period variability is that object zeta is a PMS delta Scuti (pulsational) variable. A few PMS  $\delta$  Scuti pulsators have been identified and some new possible members have also been proposed (Rodríguez & Breger 2001; Zwintz et al. 2005; Kallinger et al. 2008). Breger (1972) identified two PMS  $\delta$  Scuti variables in NGC2264 – both have colors of F stars, periods of order 3 hours and V band light curve amplitudes of order 0.05 mag.

If the J band flux of IC1396A-47 were photospheric, an  $A(V)$  of 50 mag would be required to allow zeta to have the minimum mass to fall within the instability strip at 0.5 Myr (Marconi & Palla 1998). If the Ch.4 flux is purely photospheric (see Sec. 6), the derived mass for this object is  $\sim 4$ - $4.5M_{\odot}$  (spectral type F3 and implied  $A_V=35$ ) which is compatible with it being in the instability strip.

## 7. SUMMARY AND CONCLUSIONS

We have conducted a variability study using Spitzer/IRAC data keeping in mind that mid-IR variability probes different physical mechanisms than variability in the optical or near-IR. Because IRAC is sensitive to the dust in the inner disk and envelope, variability at IRAC wavelengths in YSOs should primarily trace changes in the heating and fluctuations in the structure of the circumstellar disk and envelope surrounding the nascent star whereas optical and near-IR variability is directly related to the central object. Detailed IRAC light curves thus have the potential to allow us to construct models of the structure of the inner disk and the temporal variations in disk structure and mass accretion. Some of these variations could be tied to either the formation or migration of planets (Ida & Lin 2008). Therefore, mid-IR variability offers a new means to infer how stars are assembled and the possible early stages of planet formation.

Our photometric monitoring program on the IC1396A dark globule focuses on studying the mid-IR variability of the heavily embedded YSOs present in that area. Observations were performed with Spitzer/IRAC using two different setups corresponding to distinct timespan and temporal cadences: i) light curves covering a 14 day timespan with a twice daily cadence for 69 YSOs, and ii) continuous light curves with approximately 12 second cadence over 7 hours for 38 YSOs. Typical accuracies for our relative photometry were of order 3 mmag for the short term data, and around 10 mmag for the longer term data. This is the only star-forming region for which such extensive time series photometry has been obtained with Spitzer.

Around 60% of our sample of YSOs (69 objects) were determined to be variable on long timescales and 8 objects (out of the 38 objects with continuous light curves over a 7 hr timespan) are also labeled as variable in short timescales. We have found very different shapes in the long term light curves but the most noticeable characteristic is the very good similarity among the light curves in different bandpasses both in shape and in the amplitude of the variation. About 30%

of our total sample of YSOs show periodic-like, colorless variability with amplitudes up to about 0.2 mag. These quasi-periodic objects are about equally divided between Class I and Class II and have possible masses ranging from 0.2 to  $\sim 4.0 M_{\odot}$  (depending on the assumed extinction). We have investigated different scenarios to understand the cause of this type of variability, variable accretion, hot and cold spots in the photosphere of the objects, and variable obscuration produced by the circumstellar disk. We believe that the most plausible cause of variability for these objects are hot spots on the photosphere of our targets which asymmetrically heat the inner wall of the disk (Fig. 21). Disk warping can enhance this effect (Fig. 22). We have used radiation transfer models to check this scenario and the models are able to reproduce the observed variability in the four IRAC bands with only small changes in accretion and/or inclination angle needed to get the range of amplitudes found in our YSOs.

One of our targets, IC1396A-47, was the only one also showing periodic short term variation with an apparent  $\sim 3.5$  hr periodicity and an amplitude of order 0.04 mag. We propose that IC1396A-47 is a PMS delta Scuti variable. A dedicated, long duration photometric monitoring campaign on this object could in principle determine its mass and age from its pulsation frequencies, thereby testing theoretical PMS models at very young ages.

In addition to the variability study we have searched for new IC1396A candidate members using two different methodologies. On the one hand, we co-added the observations to obtain a deeper mosaic and extracted 15 new candidate members, 13 out of them fall into the Class II region in the IRAC color-color diagram and 2 are classified as Class I objects. On the other hand, we have searched for variability, as an indicator of youth, in the field and have detected around 50 possible new Class III candidates.

These observations have shown that Spitzer/IRAC is an exquisite instrument to carry out very accurate photometric monitorings both in timescales of hours and days. During the post-cryogenic operations, it will be the prime means to carry out this type of studies until the arrival of the James Webb Space Telescope.

This work is based [in part] on observations made with the Spitzer Space Telescope, which is operated by the Jet Propulsion Laboratory, California Institute of Technology under a contract with NASA. This research has been funded by the NASA grant JPL101185-07.E.7991.020.6, and the Spanish grants MEC/ESP 2007-65475-C02-02, MEC/Consolider-CSD2006-0070, and CAM/PRICIT-S-0505/ESP/0361. MMC acknowledges the support by a predoctoral "Calvo Rodeés" fellowship by INTA.

*Facilities:* Spitzer (IRAC)

## REFERENCES

- Allen, L. E., Calvet, N., D’Alessio, P., et al. 2004, *ApJS*, 154, 363
- Bouvier, J., Bertout, C., & Bouchet, P. 1986, *A&A*, 158, 149
- Bouvier, J., Forestini, M., & Allain, S. 1997, *A&A*, 326, 1023
- Bouvier, J., Grankin, K. N., Alencar, S. H. P., et al. 2003, *A&A*, 409, 169
- Breger, M. 1972, *ApJ*, 171, 539
- Byrne, P. B., Doyle, J. G., Brown, A., Linsky, J. L., & Rodono, M. 1987, *A&A*, 180, 172
- Carpenter, J. M., Hillenbrand, L. A., & Skrutskie, M. F. 2001, *AJ*, 121, 3160
- Castelli, F., Gratton, R. G., & Kurucz, R. L. 1997, *A&A*, 318, 841
- Charbonneau, D., Allen, L. E., Megeath, S. T., et al. 2005, *ApJ*, 626, 523
- Contreras, M. E., Sicilia-Aguilar, A., Muzerolle, J., et al. 2002, *AJ*, 124, 1585
- Cutri, R. M., Skrutskie, M. F., van Dyk, S., et al. 2003, 2MASS All Sky Catalog of point sources. (The IRSA 2MASS All-Sky Point Source Catalog, NASA/IPAC Infrared Science Archive. <http://irsa.ipac.caltech.edu/applications/Gator/>)
- D’Alessio, P., Merín, B., Calvet, N., Hartmann, L., & Montesinos, B. 2005, *Revista Mexicana de Astronomía y Astrofísica*, 41, 61
- Deming, D., Harrington, J., Laughlin, G., et al. 2007, *ApJ*, 667, L199
- Ida, S. & Lin, D. N. C. 2008, *ApJ*, 673, 487
- Kallinger, T., Zwintz, K., & Weiss, W. 2008, *A&A*, 488, 279
- Lada, C. J., Muench, A. A., Luhman, K. L., et al. 2006, *AJ*, 131, 1574
- Marconi, M. & Palla, F. 1998, *ApJ*, 507, L141
- Megeath, S. T., Allen, L. E., Gutermuth, R. A., et al. 2004, *ApJS*, 154, 367
- Morales-Calderón, M., Stauffer, J. R., Kirkpatrick, J. D., et al. 2006, *ApJ*, 653, 1454
- Reach, W. T., Megeath, S. T., Cohen, M., et al. 2005, *PASP*, 117, 978
- Reach, W. T., Rho, J., Young, E., et al. 2004, *ApJS*, 154, 385
- Robitaille, T. P., Whitney, B. A., Indebetouw, R., & Wood, K. 2007, *ApJS*, 169, 328
- Rodríguez, E. & Breger, M. 2001, *A&A*, 366, 178

- Rydgren, A. E. & Vrba, F. J. 1983, *ApJ*, 267, 191
- Scargle, J. D. 1982, *ApJ*, 263, 835
- Sicilia-Aguilar, A., Hartmann, L., Calvet, N., et al. 2006, *ApJ*, 638, 897
- Siess, L., Dufour, E., & Forestini, M. 2000, *A&A*, 358, 593
- Stetson, P. B. 1996, *PASP*, 108, 851
- Vrba, F. J., Rydgren, A. E., Chugainov, P. F., Shakovskaia, N. I., & Zak, D. S. 1986, *ApJ*, 306, 199
- Whitney, B. A., Wood, K., Bjorkman, J. E., & Cohen, M. 2003a, *ApJ*, 598, 1079
- Whitney, B. A., Wood, K., Bjorkman, J. E., & Wolff, M. J. 2003b, *ApJ*, 591, 1049
- Wood, K. & Whitney, B. 1998, *ApJ*, 506, L43
- Zwintz, K., Marconi, M., Reegen, P., & Weiss, W. W. 2005, *MNRAS*, 357, 345

Table 1. New candidates photometry from the co-added deep mosaics.

Object <sup>a</sup>	RA(J2000), DEC(J2000)	J <sup>b</sup> eJ	H <sup>b</sup> eH	$K_s$ <sup>b</sup> e $K_s$	[3.6] e[3.6]	[4.5] e[4.5]	[5.8] e[5.8]	[8.0] e[8.0]	[24] e[24]	Class
IC1396A-60	21:36:47.18 +57:29:52.6	14.184 <sup>c</sup> –	14.073 0.058	12.63 0.028	10.419 0.003	9.874 0.003	9.419 0.008	8.846 0.02	– –	II
IC1396A-61	21:36:47.63 +57:29:54.1	13.568 <sup>c</sup> –	12.342 0.042	11.655 0.033	10.426 0.004	9.964 0.004	9.545 0.01	8.972 0.031	– –	II
IC1396A-62	21:37:14.51 +57:28:40.9	14.511 0.039	13.559 0.041	12.954 0.034	11.839 0.002	11.349 0.002	11.128 0.002	10.609 0.01	7.012 0.039	II
IC1396A-63	21:37:17.42 +57:29:27.5	14.122 0.043	13.135 0.043	12.583 0.037	11.859 0.003	11.436 0.004	11.104 0.003	10.249 0.008	7.165 0.054	II
IC1396A-64 <sup>d</sup>	21:37:17.37 +57:29:20.8	14.091 <sup>c</sup> –	13.557 0.071	13.13 <sup>c</sup> –	12.901 0.012	12.669 0.013	12.344 0.011	11.528 0.023	– –	II
IC1396A-65	21:36:42.49 +57:25:23.3	14.806 0.043	14.089 0.047	13.758 0.049	13.194 0.007	12.956 0.007	12.553 0.01	11.928 0.041	8.959 0.158	II
IC1396A-66	21:37:05.87 +57:32:12.5	15.13 0.051	14.284 0.059	14.139 0.078	13.372 0.012	13.086 0.012	12.8 0.066	11.953 0.123	– –	II
IC1396A-67	21:35:58.52 +57:29:15.1	16.582 0.167	15.373 0.125	14.632 0.1	13.537 0.019	13.088 0.013	12.534 0.04	11.556 0.121	– –	II
IC1396A-68	21:36:56.26 +57:29:52.3	18.527 <sup>c</sup> –	16.098 <sup>c</sup> –	15.2 0.141	13.577 0.03	12.981 0.022	12.15 0.096	11.126 0.224	– –	II
IC1396A-69	21:36:38.03 +57:26:57.9	15.604 0.072	14.893 0.073	14.523 0.08	13.58 0.009	13.158 0.007	12.796 0.011	11.979 0.02	8.179 0.137	II
IC1396A-70	21:36:12.60 +57:31:26.3	16.504 0.132	16.161 <sup>c</sup> –	15.136 0.14	14.006 0.019	13.481 0.012	13.34 0.077	12.429 0.195	– –	II
IC1396A-71	21:36:40.34 +57:25:45.7	16.271 0.094	15.203 0.099	14.867 0.113	14.059 0.009	13.618 0.008	13.203 0.016	12.366 0.022	9.051 0.149	II
IC1396A-72	21:36:18.97 +57:29:05.1	– –	– –	– –	14.197 0.014	13.157 0.007	12.29 0.022	11.297 0.059	– –	I
IC1396A-73	21:37:11.78 +57:30:34.9	16.175 0.115	15.52 <sup>c</sup> –	14.928 0.148	14.289 0.013	13.823 0.015	13.372 0.036	12.462 0.057	6.305 0.072	II
IC1396A-74	21:36:36.35 +57:32:09.3	– –	– –	– –	15.505 0.085	14.679 0.02	13.237 0.104	11.606 0.101	– –	I

<sup>a</sup>Sicilia-Aguilar et al. (2006) identified 57 YSOs in this region and there are another 2 objects that were identified by Reach et al. (2005) thus we name our new candidate members beginning with number 60.

<sup>b</sup>Photometry for the J, H and  $K_s$  bandpasses has been taken from the 2MASS database (Cutri et al. 2003).

<sup>c</sup>Upper limits

<sup>d</sup>This object is very faint at 24  $\mu\text{m}$  and it is located too close to a brighter object to derive a reliable magnitude.

Table 2. Long-term variability: Main results from mapping data.

Object <sup>a</sup>	RA DEC		Class <sup>b</sup> SA06	ID,Class <sup>c</sup> R04	Class <sup>d</sup>	3.6 μm				4.5 μm				Jindex	Var Final
	hr, deg	(J2000)				mag	RMS	χ <sup>2</sup>	T <sub>var</sub> (days)	mag	RMS	χ <sup>2</sup>	T <sub>var</sub> (days)		
IC1396A-1	21:35:57.93	+57:29:09.9	II	ξ,I/II	I <sup>f</sup>	13.378±0.015	0.101	V	-	12.752±0.017	0.106	V	-	2.46	V
IC1396A-2	21:35:59.05	+57:30:23.3	II		II	12.516±0.012	0.023	V	-	12.200±0.013	0.026	V	-	0.33	V
IC1396A-3	21:36:06.06	+57:26:34.1	II		I <sup>f</sup>	13.010±0.015	0.02	N	-	12.567±0.016	0.024	N	-	-0.04	N
IC1396A-4	21:36:07.98	+57:26:37.1	I	γ,I/0	I	10.805±0.006	0.061	V	-	9.026±0.009	0.048	V	-	2.20	V
IC1396A-5	21:36:03.89	+57:27:12.1	II		II	11.710±0.009	0.009	N	-	11.652±0.009	0.014	N	-	0.02	N
IC1396A-6	21:36:07.46	+57:26:43.6	I		I	12.836±0.013	0.032	V	4.9	11.027±0.009	0.022	V	5.1	1.01	V
IC1396A-7	21:36:18.36	+57:28:31.6	I	ε,I/0	I	12.744±0.012	0.079	V	-	10.701±0.009	0.083	V	-	3.22	V
IC1396A-8	21:36:19.42	+57:28:38.5	I	δ,I/0	I	12.792±0.012	0.033	V	-	11.050±0.009	0.023	V	-	0.39	V
IC1396A-9 <sup>e</sup>	21:36:14.20	+57:27:37.9	II		III <sup>f</sup>	8.972±0.006	0.027	N	-	8.893±0.009	0.009	N	-	-0.03	N
IC1396A-10 <sup>e</sup>	21:36:14.20	+57:27:57.7	II		II	13.531±0.016	0.034	N	-	13.610±0.028	0.036	N	-	0.07	N
IC1396A-11	21:36:16.64	+57:28:40.4	I		I	12.502±0.012	0.025	V	-	11.751±0.009	0.022	V	-	0.31	V
IC1396A-12	21:36:16.99	+57:26:39.9	II		II	12.852±0.012	0.02	N	-	12.501±0.015	0.012	N	-	0.01	N
IC1396A-13	21:36:23.68	+57:32:45.2	II		II	12.589±0.012	0.075	V	9.1	12.374±0.014	0.071	V	9.1	0.88	V
IC1396A-14	21:36:25.07	+57:27:50.2	II		II	12.545±0.012	0.039	V	-	12.041±0.012	0.05	V	-	1.14	V
IC1396A-15 <sup>e</sup>	21:36:33.00	+57:28:49.3	II		II	13.765±0.018	0.029	V	-	13.355±0.024	0.044	V	-	0.36	V
IC1396A-16	21:36:35.31	+57:29:31.1	II		II	11.356±0.006	0.038	V	-	10.993±0.009	0.042	V	-	1.61	V
IC1396A-17	21:36:36.91	+57:31:32.6	II	ι,II	II	11.102±0.006	0.033	V	-	10.625±0.009	0.035	V	-	0.81	V
IC1396A-18	21:36:38.41	+57:29:17.4	II		II	11.353±0.006	0.049	V	-	10.975±0.009	0.039	V	-	0.97	V
IC1396A-19	21:36:39.15	+57:29:53.3	II	θ,II	II	8.581±0.006	0.071	V	-	7.859±0.009	0.064	V	-	0.06	N
IC1396A-20	21:36:41.46	+57:30:27.8	II		II	12.773±0.012	0.017	N	-	12.383±0.014	0.014	N	-	0.12	N
IC1396A-21	21:36:41.65	+57:32:17.5	II		I <sup>f</sup>	12.653±0.012	0.03	V	-	12.165±0.012	0.032	V	-	0.53	V
IC1396A-22	21:36:43.98	+57:29:28.7	II		II	11.301±0.006	0.069	V	8.2	10.761±0.009	0.047	V	9	1.71	V
IC1396A-23 <sup>e</sup>	21:36:44.00	+57:28:46.8	II		II	12.416±0.009	0.016	N	-	12.420±0.014	0.015	N	-	0.08	N
IC1396A-24	21:36:45.96	+57:29:33.9	I		I	9.644±0.006	0.056	V	6	9.114±0.009	0.064	V	6	2.88	V
IC1396A-25	21:36:46.60	+57:29:38.4	I	α,I	I	10.217±0.006	0.011	N	-	8.776±0.009	0.012	N	-	0.42	N
IC1396A-28 <sup>e</sup>	21:36:47.88	+57:31:30.6	I		I	12.137±0.009	0.059	V	5.4	11.862±0.009	0.043	V	-	0.67	V
IC1396A-29	21:36:49.41	+57:31:22.0	II		II	9.446±0.006	0.04	V	7.8	9.031±0.009	0.034	V	-	1.06	V
IC1396A-30	21:36:50.72	+57:31:10.6	II	LkHa349a,III	III <sup>f</sup>	8.688±0.006	0.033	V	-	8.439±0.009	0.035	V	-	2.3E-4	N
IC1396A-31	21:36:52.81	+57:29:43.8	II		II	12.572±0.012	0.011	N	-	12.269±0.013	0.011	N	-	0.08	N
IC1396A-32 <sup>e</sup>	21:36:54.50	+57:30:05.1	II		III <sup>f</sup>	10.108±0.006	0.019	N	-	9.889±0.009	0.006	N	-	-0.01	N
IC1396A-33 <sup>e</sup>	21:36:54.75	+57:31:45.0	II		II	13.354±0.015	0.03	N	-	-	-	-	-	0.40	N
IC1396A-34	21:36:54.89	+57:30:00.3	I	λ,I	I	11.932±0.009	0.042	V	-	11.251±0.009	0.037	V	-	0.89	V
IC1396A-35	21:36:55.20	+57:30:30.1	II	β,II	II	9.811±0.006	0.053	V	-	9.309±0.009	0.033	V	-	0.57	V
IC1396A-36	21:36:55.43	+57:31:39.1	II		III <sup>f</sup>	11.222±0.006	0.009	N	-	11.187±0.009	0.008	N	-	0.04	N
IC1396A-37	21:36:56.98	+57:29:22.7	II		II	11.569±0.009	0.049	V	9.1	11.049±0.009	0.041	V	9.1	1.18	V
IC1396A-38	21:36:57.67	+57:27:33.1	II		II	9.447±0.006	0.033	V	-	8.987±0.009	0.049	V	-	1.12	V
IC1396A-39	21:36:57.83	+57:30:56.1	I	η,I	I	12.186±0.009	0.057	V	7.8	11.139±0.009	0.058	V	9	2.26	V
IC1396A-40	21:36:57.93	+57:29:10.7	I	ν,I/II	II <sup>f</sup>	10.316±0.006	0.025	V	6	9.916±0.009	0.027	V	7.6	0.60	V
IC1396A-41	21:36:58.90	+57:30:29.2	I		I	12.865±0.012	0.032	V	-	12.211±0.013	0.027	V	-	0.19	V
IC1396A-43	21:36:59.47	+57:31:34.9	II		II	11.739±0.009	0.055	V	10.5	11.251±0.009	0.063	V	-	1.90	V
IC1396A-44 <sup>e</sup>	21:37:01.05	+57:30:39.7	I		I	13.257±0.015	0.023	N	-	13.110±0.021	0.026	N	-	-0.06	N
IC1396A-45	21:37:01.91	+57:28:22.2	II		II	10.856±0.006	0.027	V	6	10.535±0.009	0.034	V	6	0.28	V
IC1396A-46	21:37:02.00	+57:31:55.3	II		II	12.061±0.009	0.017	N	-	11.911±0.009	0.015	N	-	0.13	N
IC1396A-47	21:37:02.32	+57:31:15.2	I	ζ,I	I	10.790±0.006	0.065	V	9	9.807±0.009	0.078	V	9	3.86	V
IC1396A-49	21:37:06.49	+57:32:31.6	II		II	10.900±0.006	0.064	V	-	10.459±0.009	0.068	V	-	2.06	V
IC1396A-50	21:37:07.18	+57:31:27.8	I		I	13.585±0.016	0.04	V	-	12.718±0.017	0.027	V	-	0.21	V
IC1396A-51 <sup>e</sup>	21:37:07.71	+57:32:11.0	II		II	12.923±0.012	0.042	V	-	12.666±0.016	0.052	V	-	0.23	N
IC1396A-53	21:37:09.36	+57:29:48.3	II		II	10.973±0.006	0.019	V	-	10.515±0.009	0.028	V	-	0.74	V
IC1396A-54	21:37:09.44	+57:30:36.7	II		II	12.125±0.009	0.035	V	-	11.817±0.009	0.047	V	-	0.72	V

Table 2—Continued

Object <sup>a</sup>	RA DEC hr, deg (J2000)		Class <sup>b</sup> SA06	ID,Class <sup>c</sup> R04	Class <sup>d</sup>	3.6 $\mu\text{m}$				4.5 $\mu\text{m}$				Jindex	Var Final
						mag	RMS	$\chi^2$	$T_{var}$ (days)	mag	RMS	$\chi^2$	$T_{var}$ (days)		
IC1396A-55	21:37:10.13	+57:31:26.6	II		II	13.252±0.015	0.029	N	-	12.918±0.019	0.029	N	-	0.24	N
IC1396A-56	21:37:10.31	+57:30:18.9	II		II	11.545±0.009	0.011	N	-	11.417±0.009	0.017	N	-	0.17	N
IC1396A-57	21:37:10.54	+57:31:12.4	II		II	11.130±0.006	0.058	V	-	10.724±0.009	0.063	V	-	2.19	V
IC1396A-58	21:36:56.51	+57:31:51.6	-	$\kappa, \text{II}$	II	12.323±0.009	0.016	N	-	11.626±0.009	0.015	N	-	0.05	N
IC1396A-59	21:37:03.04	+57:30:48.7	-	$\mu, \text{I}$	I	13.564±0.016	0.032	N	-	12.218±0.013	0.036	N	-	0.48	N
IC1396A-60	21:36:47.18	+57:29:52.6	-		II	10.406±0.006	0.062	V	-	9.869±0.009	0.04	V	-	1.83	V
IC1396A-61	21:36:47.63	+57:29:54.1	-		II	10.416±0.006	0.030	V	-	9.960±0.009	0.033	V	-	1.30	V
IC1396A-62	21:37:14.51	+57:28:40.9	-		II	11.833±0.009	0.061	V	-	-	-	-	-	1.96	V
IC1396A-63	21:37:17.42	+57:29:27.5	-		II	11.835±0.009	0.038	V	-	-	-	-	-	1.01	V
IC1396A-64	21:37:17.37	+57:29:20.8	-		II	12.886±0.012	0.019	N	-	-	-	-	-	0.10	N
IC1396A-65	21:36:42.49	+57:25:23.3	-		II	13.176±0.015	0.018	N	-	12.943±0.019	0.036	N	-	0.16	N
IC1396A-66	21:37:05.87	+57:32:12.5	-		II	13.362±0.015	0.044	V	9	13.074±0.021	0.033	N	-	0.25	V
IC1396A-67	21:35:58.52	+57:29:15.1	-		II	13.546±0.016	0.036	N	-	13.098±0.021	0.027	N	-	0.15	N
IC1396A-68	21:36:56.26	+57:29:52.3	-		II	13.551±0.016	0.023	N	-	12.974±0.02	0.024	N	-	0.09	N
IC1396A-69	21:36:38.03	+57:26:57.9	-		II	13.578±0.016	0.048	V	-	13.172±0.022	0.077	V	-	0.90	V
IC1396A-70	21:36:12.60	+57:31:26.3	-		II	13.997±0.021	0.126	V	-	13.473±0.026	0.095	V	-	1.08	V
IC1396A-71	21:36:40.34	+57:25:45.7	-		II	14.038±0.022	0.043	N	-	13.617±0.028	0.042	N	-	0.34	N
IC1396A-72	21:36:18.97	+57:29:05.1	-		I	14.186±0.024	0.051	V	-	-	-	-	-	0.13	N
IC1396A-73	21:37:11.78	+57:30:34.9	-		II	14.269±0.026	0.051	N	-	13.823±0.031	0.051	N	-	0.26	N
IC1396A-74	21:36:36.35	+57:32:09.3	-		I	15.491±0.059	0.053	N	-	14.663±0.050	0.040	N	-	-0.05	V

<sup>a</sup>Objects are named following the order in Table 6 of Sicilia-Aguilar et al. (2006) (Note that not all their members are included), objects -58 and -59 are YSOs from Reach et al. (2004) not in common with Sicilia-Aguilar et al. (2006), and objects from -60 to -74 are our new candidate members from Table 1.

<sup>b</sup>YSO Class as in Sicilia-Aguilar et al. (2006).

<sup>c</sup>ID and YSO Class as in Reach et al. (2004).

<sup>d</sup>YSO Class in this paper. Members in Sicilia-Aguilar et al. (2006) that do not show IR excess in our data have been classified as Class III.

<sup>e</sup>Uncertain cluster members following Sicilia-Aguilar et al. (2006).

<sup>f</sup>Classification in disagreement with Sicilia-Aguilar et al. (2006).

Table 3. Time series in the four IRAC bands for the variable YSOs of our sample. (Full table available in the electronic version of this article.)

Object	MJD (days)	[3.6] e[3.6]	[4.5] e[4.5]	[5.8] e[5.8]	[8.0] e[8.0]
IC1396A-1	54488.6878678	13.233 0.018	12.596 0.013	11.833 0.023	10.448 0.042
IC1396A-1	54489.2077075	13.149 0.014	12.545 0.012	11.741 0.028	10.365 0.037
IC1396A-1	54489.5421136	13.178 0.019	12.529 0.011	11.730 0.020	10.415 0.038
IC1396A-1	54490.0224986	13.229 0.019	12.583 0.012	11.842 0.026	10.405 0.037
IC1396A-1	54490.3616676	13.212 0.020	12.572 0.012	11.760 0.019	10.360 0.035
IC1396A-1	54490.7798051	13.256 0.021	12.585 0.011	11.800 0.024	10.340 0.035
IC1396A-1	54491.2620497	13.293 0.021	12.682 0.014	11.867 0.024	10.501 0.036
IC1396A-1	54491.6974542	13.384 0.023	12.774 0.014	12.000 0.030	10.531 0.040
IC1396A-1	54492.3575716	13.428 0.027	12.836 0.014	12.065 0.030	10.604 0.036
IC1396A-1	54492.8026341	13.424 0.028	12.783 0.013	12.037 0.030	10.633 0.039



Table 4. Peak-to-peak amplitudes for the 18 IC 1396A YSOs which present periodic-like, colorless variations. Long term data.

Object	Peak-to-peak Amplitudes (mag)			
	3.6 $\mu\text{m}$	4.5 $\mu\text{m}$	5.8 $\mu\text{m}$	8.0 $\mu\text{m}$
IC 1396A-4	0.15	0.11	0.09	0.07
IC 1396A-6 <sup>a</sup>	0.09	0.07	0.15	–
IC 1396A-7	0.19	0.19	0.17	0.15
IC 1396A-13 <sup>a</sup>	0.17	0.17	0.23	–
IC 1396A-14	0.09	0.11	0.14	0.15
IC 1396A-15 <sup>b</sup>	0.12	0.12	0.49	0.53
IC 1396A-16 <sup>b</sup>	0.09	0.09	0.2	0.15
IC 1396A-17	0.10	0.10	0.10	0.11
IC 1396A-22	0.20	0.18	0.21	0.23
IC 1396A-24	0.11	0.12	0.11	0.11
IC 1396A-28 <sup>b</sup>	0.15	0.12	0.16	0.23
IC 1396A-29	0.06	0.06	0.04	0.05
IC 1396A-34	0.11	0.10	0.12	0.08
IC 1396A-37	0.14	0.13	0.12	0.17
IC 1396A-39	0.17	0.16	0.19	0.22
IC 1396A-40	0.07	0.07	0.06	0.06
IC 1396A-41 <sup>b</sup>	0.06	0.07	0.23	0.51
IC 1396A-43	0.16	0.16	0.17	0.18
IC 1396A-45	0.07	0.07	0.07	0.06
IC 1396A-47	0.25	0.21	0.24	0.25
IC 1396A-60	0.13	0.11	0.12	0.07
IC 1396A-61	0.08	0.09	0.11	0.09
IC 1396A-66 <sup>b</sup>	0.08	0.11	0.25	0.3

<sup>a</sup>This object is too faint to derive its amplitude at 8.0 $\mu\text{m}$ .

<sup>b</sup>The light curves of this object are much noisier at 5.8 and 8.0 $\mu\text{m}$  than at shorter wavelenths

Table 5. Short-time variability: Main results from the staring data.

Object	4.5 $\mu\text{m}$				8 $\mu\text{m}$				J index	Var Fin
	mag	RMS	$\chi^2$	$T_{var}$ (hr)	mag	RMS	$\chi^2$	$T_{var}$ (hr)		
IC 1396-16	10.910±0.006	0.009	N	-	10.246±0.181	0.256	N	-	0.03	N
IC 1396-17	10.600±0.003	0.006	V	-	9.167±0.011	0.014	N	-	0.07	N
IC 1396-18	10.970±0.004	0.006	V	-	10.018±0.042	0.057	N	-	-0.11	N
IC 1396-20	12.368±0.007	0.010	N	-	11.323±0.068	0.093	N	-	0.02	N
IC 1396-21	12.143±0.007	0.010	N	-	10.180±0.029	0.040	N	-	0.09	N
IC 1396-22	10.585±0.003	0.033	V	-	9.742±0.031	0.046	N	-	1.69	Y
IC 1396-23	12.392±0.009	0.012	N	-	10.284±0.039	0.050	N	-	0.05	N
IC 1396-24	9.008±0.002	0.005	V	-	8.000±0.004	0.005	N	-	0.37	Y
IC 1396-25	8.739±0.002	0.003	N	-	6.614±0.002	0.006	V	-	0.56	N
IC 1396-28	11.910±0.015	0.018	N	-	8.558±0.037	0.053	N	-	-0.01	N
IC 1396-29	9.009±0.002	0.003	N	-	7.941±0.005	0.007	N	-	0.09	N
IC 1396-31	12.245±0.006	0.009	N	-	11.187±0.043	0.060	N	-	0.01	N
IC 1396-32	9.870±0.002	0.003	N	-	9.690±0.023	0.032	N	-	0.01	N
IC 1396-33	13.251±0.018	0.024	N	-	10.602±0.126	0.173	N	-	0.11	N
IC 1396-34	11.266±0.005	0.012	V	-	9.749±0.009	0.013	N	-	0.42	N
IC 1396-35	9.263±0.002	0.009	V	-	8.027±0.007	0.014	V	-	1.70	Y
IC 1396-36	11.230±0.004	0.005	N	-	10.811±0.080	0.108	N	-	-0.07	N
IC 1396-37	11.027±0.004	0.006	V	-	9.931±0.020	0.025	N	-	0.02	N
IC 1396-39	10.979±0.004	0.018	V	-	8.898±0.033	0.046	N	-	0.56	Y
IC 1396-40	9.917±0.002	0.003	N	-	8.719±0.005	0.007	N	-	0.08	N
IC 1396-41	12.193±0.008	0.011	N	-	10.452±0.093	0.141	N	-	0.084	N
IC 1396-43	11.230±0.005	0.008	V	-	9.564±0.022	0.035	N	-	0.34	Y
IC 1396-44	13.116±0.017	0.024	N	-	9.001±0.017	0.021	-	-	0.03	N
IC 1396-46	11.912±0.008	0.010	N	-	-	-	-	-	0.22	N
IC 1396-47	9.722±0.003	0.011	V	3.4	8.115±0.007	0.014	V	3.4	1.45	Y
IC 1396-48	13.581±0.060	0.080	N	-	8.846±0.044	0.059	N	-	-0.04	N
IC 1396-50	12.689±0.008	0.010	N	-	10.128±0.013	0.017	N	-	0.07	N
IC 1396-51 <sup>a</sup>	-	-	-	-	12.278±0.047	0.063	N	-	-0.14	N
IC 1396-54	11.682±0.004	0.008	V	-	-	-	-	-	0.93	N
IC 1396-55	12.918±0.008	0.011	N	-	11.898±0.036	0.049	N	-	0.02	N
IC 1396-57	10.628±0.003	0.005	V	-	9.458±0.004	0.008	V	-	0.56	Y
IC 1396-58	11.586±0.004	0.006	N	-	10.088±0.027	0.037	N	-	0.06	N
IC 1396-59	12.197±0.006	0.007	N	-	10.790±0.036	0.049	N	-	-0.03	N
IC 1396-60	9.867±0.003	0.005	V	-	-	-	-	-	0.89	N
IC 1396-61	9.923±0.003	0.007	V	-	8.969±0.009	0.015	V	-	0.82	Y
IC 1396-66	13.038±0.010	0.013	N	-	11.714±0.041	0.058	N	-	-0.14	N
IC 1396-68	13.023±0.013	0.017	N	-	13.107±0.474	0.679	N	-	-0.09	N
IC 1396-74	14.663±0.038	0.050	N	-	11.648±0.063	0.080	N	-	-0.01	N

<sup>a</sup>The object is out of the FOV in Ch. 2.

Table 6. Photometry for the variable objects found in the field.

ID <sup>a</sup>	RA(J2000), DEC(J2000)	J <sup>b</sup> eJ	H <sup>b</sup> eH	$K_s^b$ e $K_s$	[3.6] e[3.6]	[4.5] e[4.5]	[5.8] e[5.8]	[8.0] e[8.0]
347	21:35:51.08 +57:28:12.4	15.381 0.033	14.881 0.042	14.611 0.038	14.272 0.029	14.322 0.027	13.268 0.135	11.331 0.095
751	21:36:15.20 +57:25:27.8	15.442 0.047	14.659 0.052	14.418 0.038	13.787 0.01	13.556 0.012	13.585 0.063	12.365 0.06
823	21:36:07.44 +57:26:43.4	--	--	--	12.869 0.035	11.032 0.025	9.635 0.019	8.576 0.055
1230	21:35:58.07 +57:28:50.4	15.596 0.088	15.059 0.125	14.836 0.091	13.899 0.034	14.067 0.055	13.809 0.18	--
1256	21:35:53.10 +57:29:37.1	15.208 0.031	14.709 0.047	14.499 0.036	14.424 0.025	14.407 0.027	15.228 0.417	14.529 0.908
1469	21:35:55.39 +57:29:42.8	15.654 0.034	15.059 0.042	14.857 0.049	14.688 0.028	14.673 0.032	14.603 0.207	--
1685	21:35:55.64 +57:30:03.3	15.314 0.03	14.767 0.041	14.453 0.038	14.136 0.014	14.151 0.019	14.034 0.087	--
2519	21:36:01.65 +57:30:50.0	15.598 0.041	14.957 0.052	14.701 0.041	14.146 0.017	14.02 0.018	14.082 0.137	13.755 0.269
2712	21:36:10.97 +57:29:50.7	15.649 0.034	14.601 0.037	14.256 0.027	14.11 0.019	14.067 0.022	14.204 0.319	13.246 0.835
2812	21:36:40.34 +57:25:45.6	16.292 0.049	15.439 0.063	14.862 0.04	14.102 0.015	13.688 0.016	13.187 0.042	12.506 0.047
3115	21:36:13.35 +57:30:16.2	15.697 0.039	15.111 0.052	14.854 0.05	14.716 0.039	14.635 0.035	14.753 0.342	--
3154	21:36:17.04 +57:29:48.2	15.674 0.034	14.63 0.041	14.198 0.029	13.789 0.048	13.741 0.053	14.619 1.782	--
3367	21:36:33.20 +57:27:51.9	14.985 0.028	14.413 0.04	14.208 0.031	14.001 0.022	13.874 0.018	14.172 0.088	--
3402	21:36:16.14 +57:30:26.9	14.598 0.025	14.209 0.036	14.006 0.026	13.909 0.017	13.797 0.014	13.635 0.119	12.549 0.248
3444	21:36:17.94 +57:30:16.3	15.531 <sup>c</sup> --	15.35 0.07	15.048 0.057	14.474 0.034	14.419 0.033	--	--
3526	21:36:45.86 +57:26:22.9	15.174 0.03	14.494 0.043	14.339 0.033	14.264 0.012	14.326 0.024	14.171 0.091	13.071 0.073
3795	21:36:33.02 +57:28:49.4	16.154 0.048	14.919 0.046	14.127 0.032	13.738 0.04	13.344 0.037	12.895 0.354	12.874 1.697
4459	21:36:36.94 +57:29:28.6	15.715 0.03	15.014 0.04	14.599 0.041	14.267 0.076	14.173 0.11	12.556 0.322	--
4535	21:36:37.58 +57:29:31.7	15.468 0.03	14.983 0.038	14.816 0.045	14.444 0.078	14.431 0.105	12.978 0.176	11.433 0.221
4780	21:36:54.72 +57:27:26.7	--	--	--	16.999 0.109	16.836 0.255	--	--
5053	21:36:12.99 +57:34:05.4	15.167 0.03	14.053 0.032	13.752 0.024	13.474 0.022	13.498 0.018	13.355 0.161	13.58 0.606
5120	21:36:38.61 +57:30:27.0	17.113 0.103	15.528 0.051	14.937 0.051	14.873 0.134	14.708 0.145	--	--
5272	21:36:40.49 +57:30:25.8	15.99 0.052	14.524 0.053	13.664 <sup>c</sup> --	13.32 0.043	13.225 0.061	12.12 0.116	10.638 0.172
5290	21:36:28.43 +57:32:13.5	14.431 0.023	13.482 0.03	13.144 0.019	12.901 0.013	12.824 0.012	13.889 0.321	--
5546	21:36:47.62 +57:29:54.0	13.497 0.024	12.356 0.038	11.593 0.019	10.477 0.004	10.017 0.004	9.672 0.012	9.082 0.036
5580	21:36:25.98 +57:33:10.2	14.883 0.029	14.265 0.043	14.011 0.029	13.702 0.037	13.638 0.025	14.196 0.629	--
5610	21:36:49.03 +57:29:49.2	16.904 0.079	15.51 0.059	14.648 0.043	14.157 0.043	14.126 0.072	15.489 2.214	--
5647	21:36:44.11 +57:30:38.3	16.214 0.056	15.237 0.06	14.754 0.045	14.431 0.085	14.431 0.075	14.023 0.386	--
5676	21:36:44.71 +57:30:37.4	16.445 0.053	15.464 0.063	14.851 0.043	14.388 0.097	14.501 0.094	--	11.127 0.166
5680	21:36:16.09 +57:34:48.6	11.97 0.022	11.185 0.028	10.931 0.016	10.791 0.004	10.746 0.004	10.77 0.01	10.684 0.01
5998	21:36:45.86 +57:31:03.5	--	--	--	14.223 0.106	14.578 0.146	--	10.166 0.294
6200	21:36:53.17 +57:30:18.7	17.607 <sup>c</sup> --	16.315 0.123	15.177 0.067	14.426 0.073	14.118 0.056	14.5 1.015	--
6450	21:36:36.50 +57:33:14.3	16.876 0.079	16.196 0.125	15.781 0.092	14.815 0.116	14.933 0.098	--	--
6710	21:36:34.86 +57:33:57.1	15.135 0.026	14.478 0.031	14.251 0.031	14.171 0.016	14.175 0.021	14.063 0.087	--

Table 6—Continued

ID <sup>a</sup>	RA(J2000), DEC(J2000)	J <sup>b</sup> eJ	H <sup>b</sup> eH	$K_s$ <sup>b</sup> e $K_s$	[3.6] e[3.6]	[4.5] e[4.5]	[5.8] e[5.8]	[8.0] e[8.0]
6975	21:36:25.61 +57:35:46.2	--	--	--	14.152 0.058	14.068 0.051	14.586 0.365	--
7003	21:36:52.64 +57:31:50.4	15.005 0.029	13.703 0.032	13.156 0.019	12.673 0.024	12.623 0.016	11.816 0.115	10.26 0.157
7159	21:36:54.58 +57:31:50.2	17.258 0.108	15.771 0.074	15.035 0.05	14.067 0.076	13.879 0.065	13.74 0.721	12.97 1.429
7377	21:37:10.55 +57:29:52.9	15.107 0.028	14.3 0.033	14.134 0.027	13.85 0.013	13.842 0.027	13.849 0.11	14.044 0.348
7491	21:36:51.54 +57:32:53.4	16.231 0.046	15.285 0.055	14.846 0.047	13.917 0.092	13.936 0.072	13.172 0.754	11.122 0.534
7493	21:36:48.84 +57:33:17.4	17.542 0.122	16.693 0.154	16.584 0.21	14.666 0.086	14.931 0.087	--	--
7532	21:36:54.66 +57:32:29.4	17.35 <sup>c</sup> --	16.177 0.105	15.27 0.08	13.858 0.075	13.85 0.052	11.82 0.127	9.94 0.124
7949	21:37:00.27 +57:32:23.8	--	--	--	14.256 0.256	14.874 0.341	11.454 0.127	9.457 0.129
8151	21:36:45.97 +57:34:55.1	15.102 0.047	14.434 0.059	14.254 0.036	13.811 0.032	13.949 0.061	14.221 0.22	--
8183	21:36:59.85 +57:32:56.2	15.636 0.037	15.23 0.049	15.003 0.053	14.843 0.048	14.686 0.049	14.55 0.323	--
8507	21:37:06.49 +57:32:32.1	13.33 0.02	12.335 0.028	11.904 0.016	10.862 0.0030	10.539 0.0030	10.201 0.0070	9.527 0.009
8689	21:37:09.39 +57:32:25.4	15.82 0.116	15.205 0.181	15.016 0.07	13.793 0.052	13.394 0.091	13.299 0.135	--

<sup>a</sup>Internal ID for each object.

<sup>b</sup>Photometry for the J, H and  $K_s$  bandpasses has been taken from the 2MASS database (Cutri et al. 2003).

<sup>c</sup>Upper limmits.

Table 7. Statistics for the long term variability.

Sample	Number of objects	% Total <sup>a</sup>
Class I in the sample	20	29
Class II in the sample	45	65
Variable objects	41	59
Class I with amplitudes $> 0.05\text{mag}$	15	22
Class II with amplitudes $> 0.05\text{mag}$	26	38
Class I with amplitudes $> 0.1\text{mag}$	11	16
Class II with amplitudes $> 0.1\text{mag}$	17	25
Periodic-like Class I	9	13
Periodic-like Class II	14	20
Color variables	3	4

<sup>a</sup>Percentage to the total sample (69 objects).

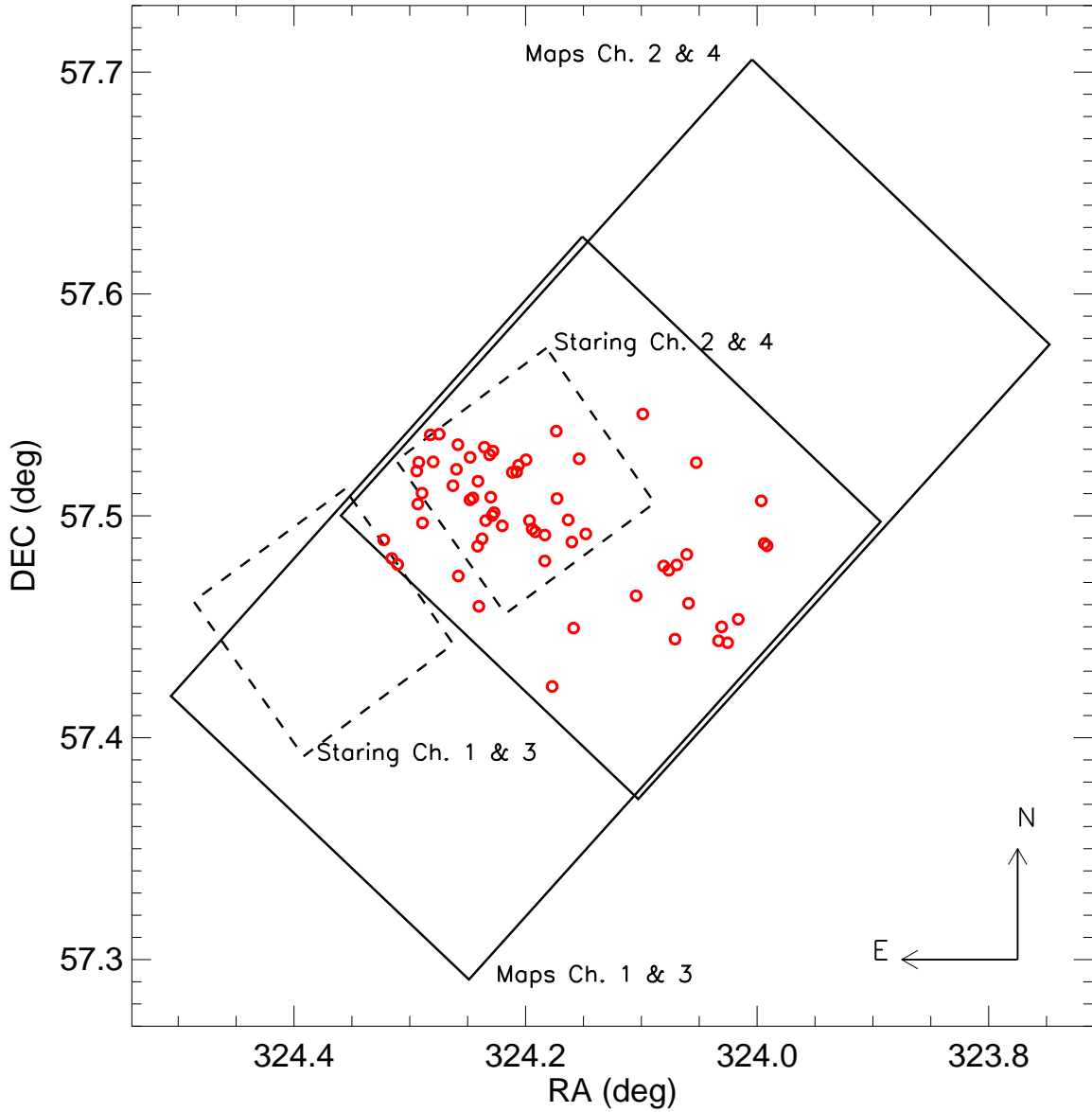


Fig. 1.— Layout of observations. YSOs from Sicilia-Aguilar et al. (2006) are marked with open circles. East is left, North is up. The solid and dashed rectangles show the field of view of the map and staring data respectively. All the previously known members are located within the area where mapping observations at Ch. 1 & 3 and Ch. 2 & 4 overlap.

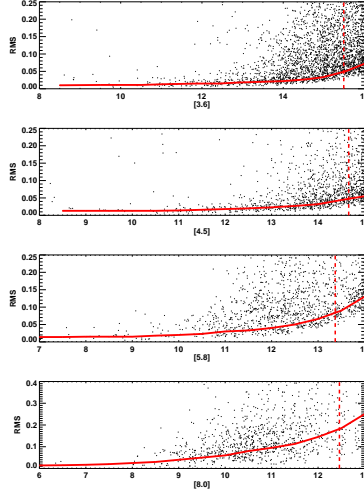


Fig. 2.— Light curve RMS versus mean magnitude for all detections in the mosaic at  $3.6 \mu\text{m}$ . The fitted polynomial (red solid line) has been used as a measure of the error. The vertical dashed line represents the magnitude of our faintest target.

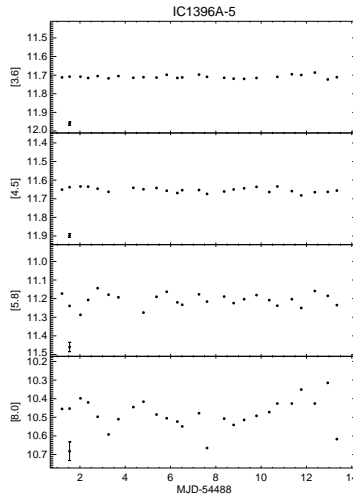


Fig. 3.— Example of a light curve for a non-variable YSO, IC1396A-5, in the four IRAC bandpasses. The RMS of the light curves is 9, 14, 34 and 80 mmag for IRAC channels 1 through 4 respectively.

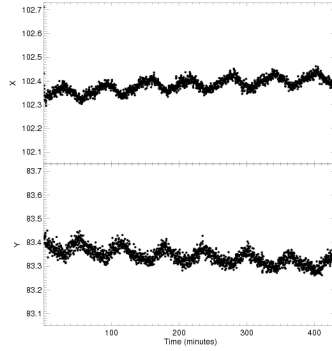


Fig. 4.— Array x-position (top) and y-position (bottom) as a function of time for one of our targets. Only the already known 3000 sec oscillation of the pointing can be seen.

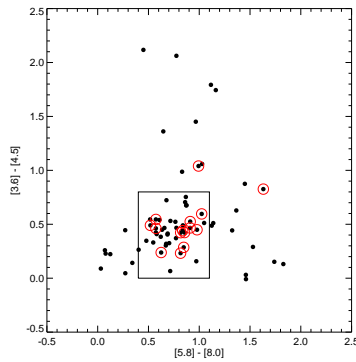


Fig. 5.— IRAC color-color diagram after Allen et al. (2004). Black filled circles represent the whole sample of YSOs and red open circles stand for our new Class I and Class II selections. Objects inside the box are classified as Class II objects while redder colors are indicative of Class I objects and objects close to (0,0) are either field objects or Class III sources (Allen et al. 2004).



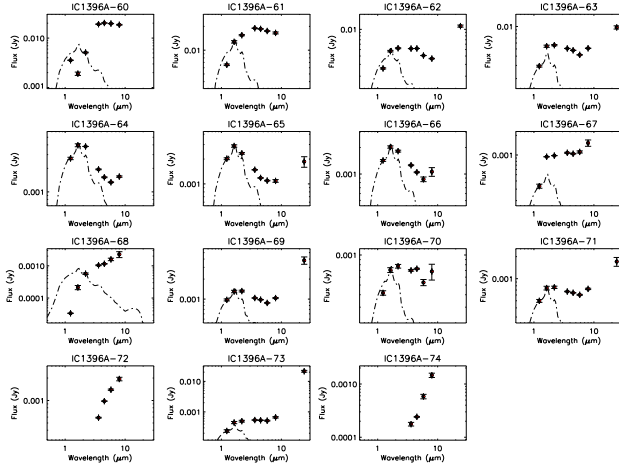


Fig. 6.— Spectral energy distributions for our new candidates. All of them have been classified as Class II or Class I objects by means of the IRAC color-color diagram and have thick disks surrounding the central object. The J, H, and  $K_s$  magnitudes come from the 2MASS database (Cutri et al. 2003). The dashed lines are Kurucz models (Castelli et al. 1997) aiming to represent the photosphere of each target assuming that the bluest 2MASS data point with good quality photometry represents the photospheric flux.

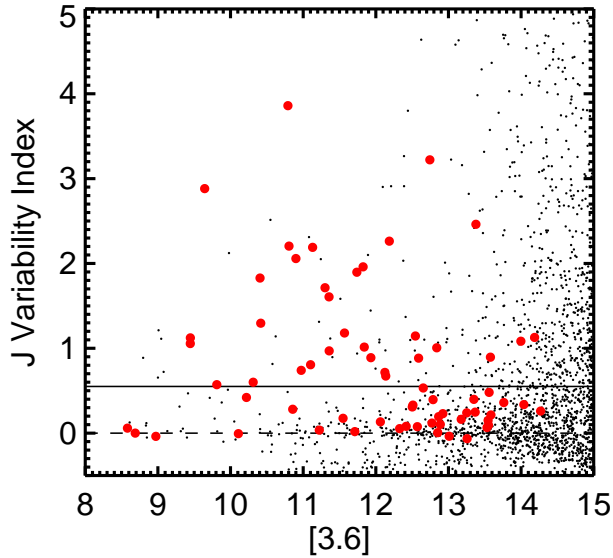


Fig. 7.— Stetson variability index (J) plotted as a function of [3.6] mean magnitude for stars brighter than [3.6]=15. The dashed line at  $J=0$  shows the expected value of the variability index for non variable stars, and the dotted line at  $J=0.55$  represents the minimum adopted value used to identify variable stars in this study. Our IC1396A YSOs are represented with red filled circles.

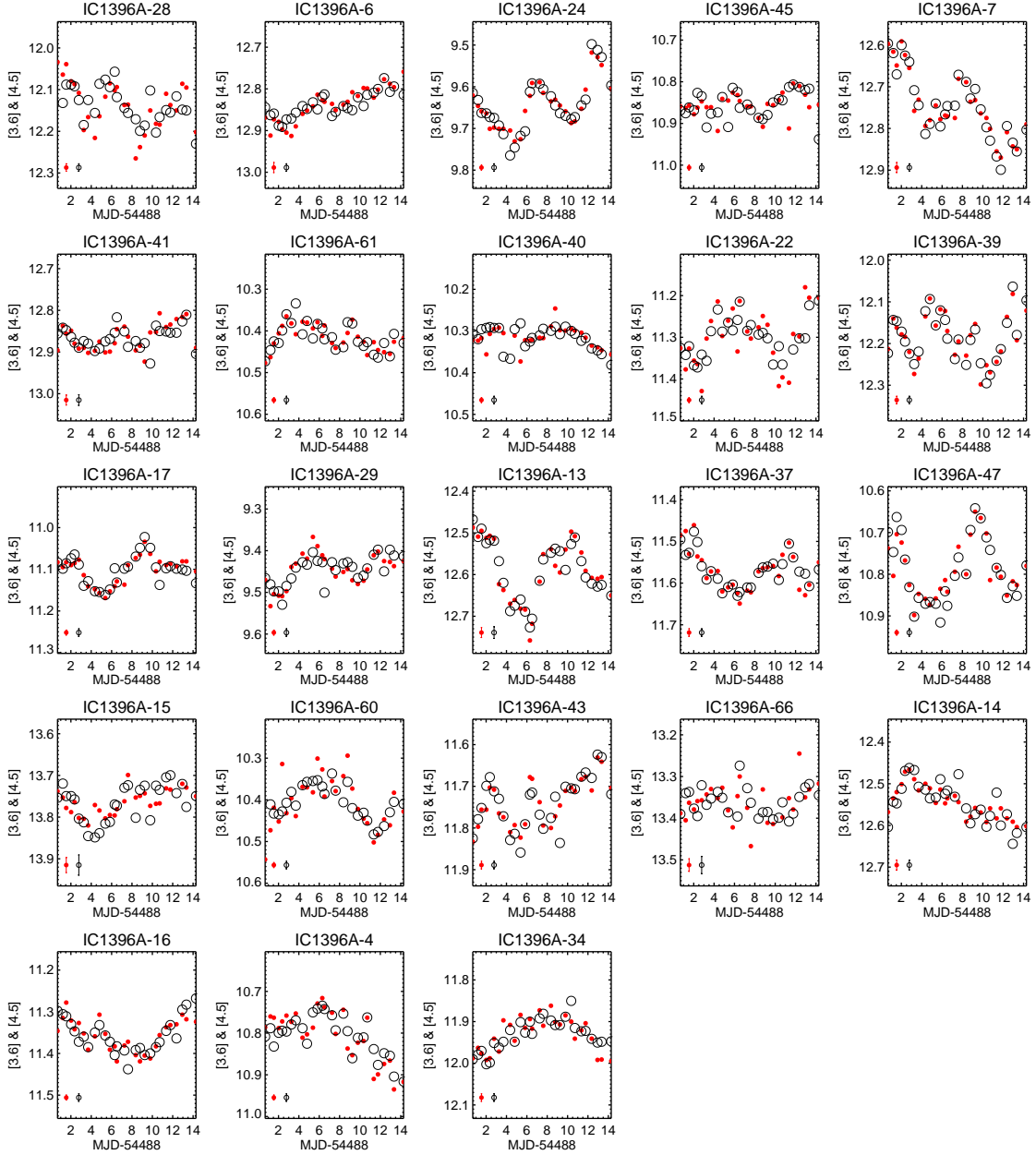


Fig. 8.— Light curves for the 18 IC1396A YSOs which present periodic-like, colorless variations. In the Figure we show objects that seem to have increasing periods (from 5 to more than 14 days) from the top left panel to the right bottom one. Red filled circles represent the Ch. 1 data while open black circles show the Ch. 2 data. The Ch. 2 light curves have been shifted in the y axis to match the mean magnitudes in Ch. 1.

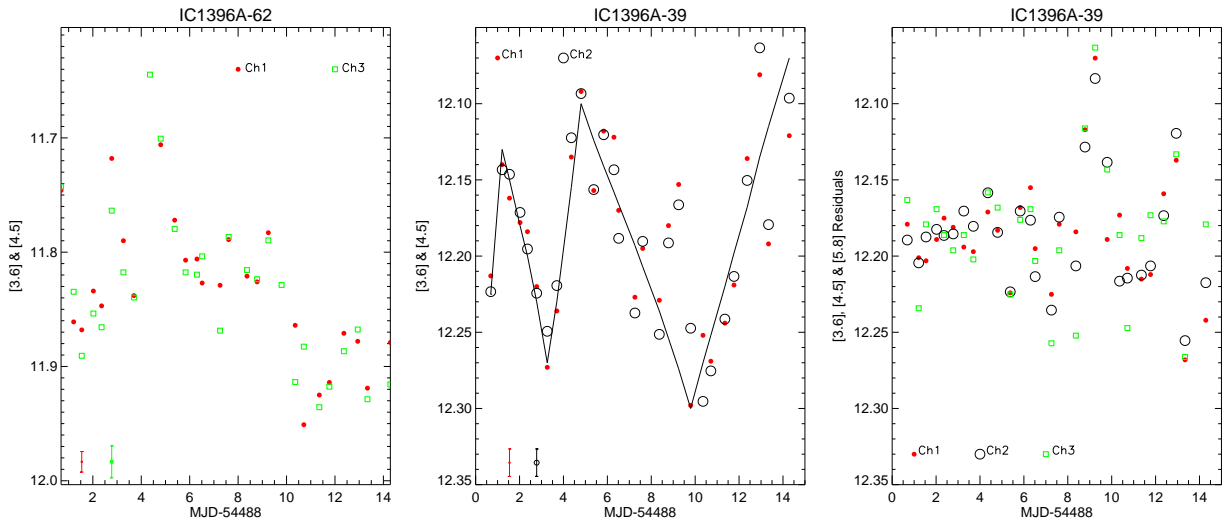


Fig. 9.— **a)** Light curves for IC1396A-62. This object shows a sudden change in brightness of about 0.2 mag that lasts for 2 days. The object is located just at the border of Ch. 2 and Ch. 4 FOV and thus the light curves presented are those for Ch. 1 (filled circles) and Ch. 3 (open squares). **b)** Light curves for IC1396A-39, Ch. 1 (red dots), Ch. 2 (black circles), with a saw-tooth pattern illustrating the long-term variation. **c)** Residuals from the light curve in (b) after subtracting the saw-tooth pattern showing a flare or accretion event. Ch. 3 data is also included (open squares).

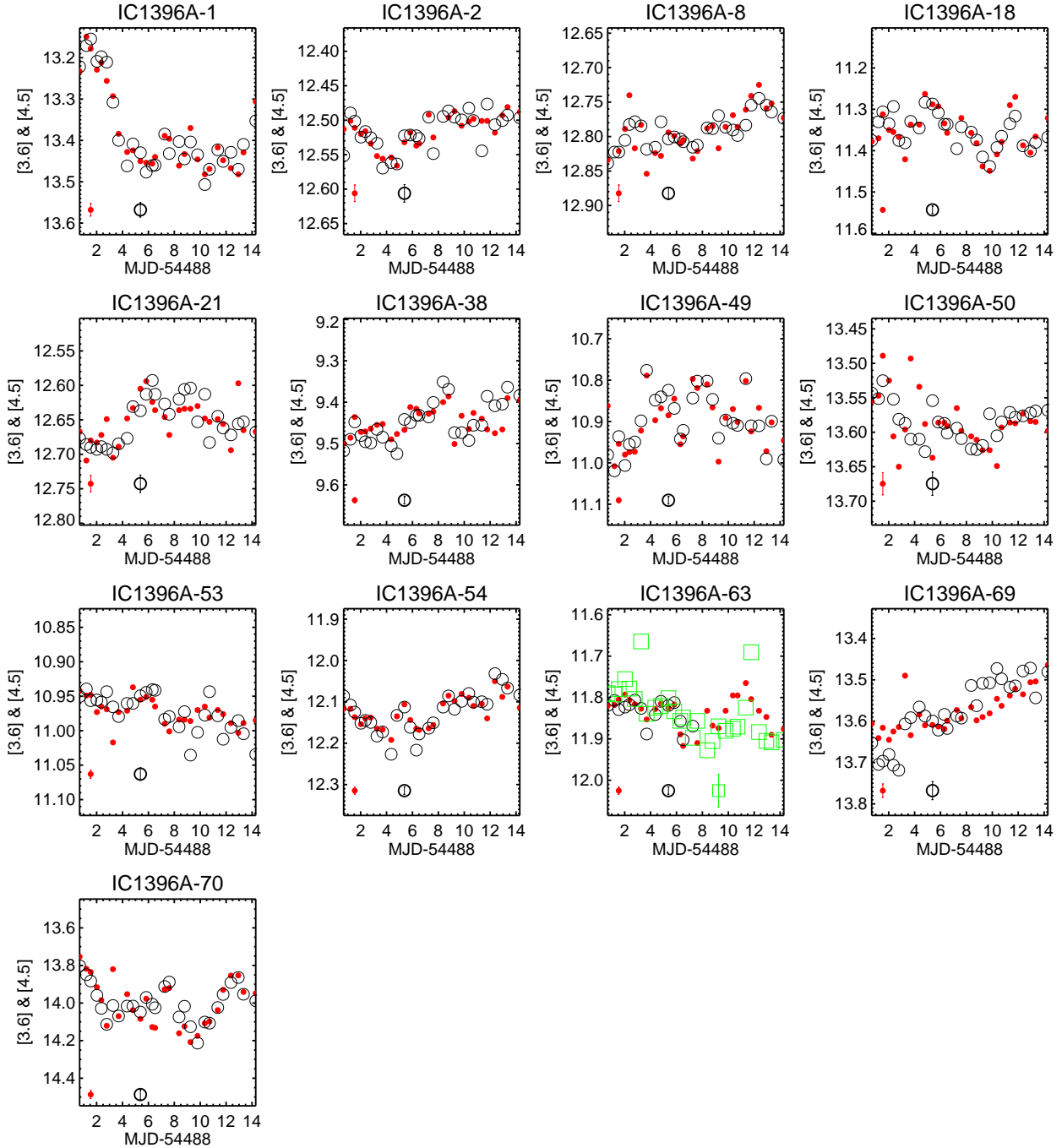


Fig. 10.— Light curves for the 18 IC1396A YSOs which show slow, non-periodic colorless variability. In the figure Ch. 1 (red filled circles) and Ch. 2 are plotted (black open circles). For object 63 the Ch. 3 data – green open squares– is also plotted.

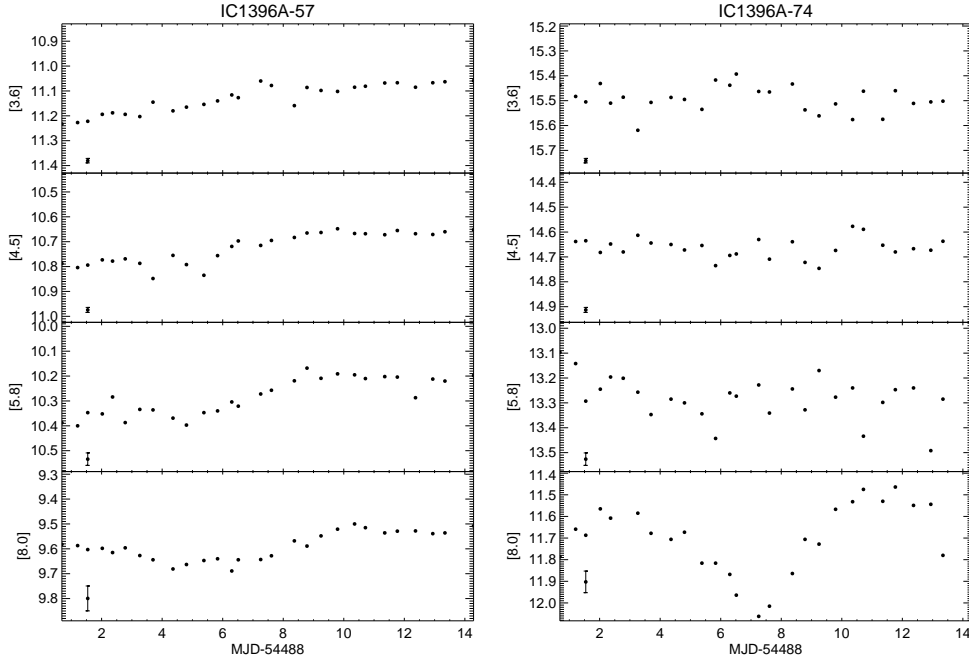


Fig. 11.— **a)** Light curves for IC1396A-57. This object shows a continuous change in shape from Ch. 1 to Ch. 4. The peak-to-peak amplitude at Ch. 4 is  $\sim 0.2$  mag. **b)** Light curves for IC1396A-74. The panels, from the top to the bottom, show the IRAC photometry at Ch. 1 ( $3.6 \mu\text{m}$ ), Ch. 2 ( $4.5 \mu\text{m}$ ), Ch. 3 ( $5.6 \mu\text{m}$ ) and Ch. 4 ( $8.0 \mu\text{m}$ ) respectively. This object shows almost constant light curves at the three bluer band passes while the star fades in brightness in Ch. 4 for  $\sim 6$  days. The amplitude of the variation is  $\sim 0.5$  mag.

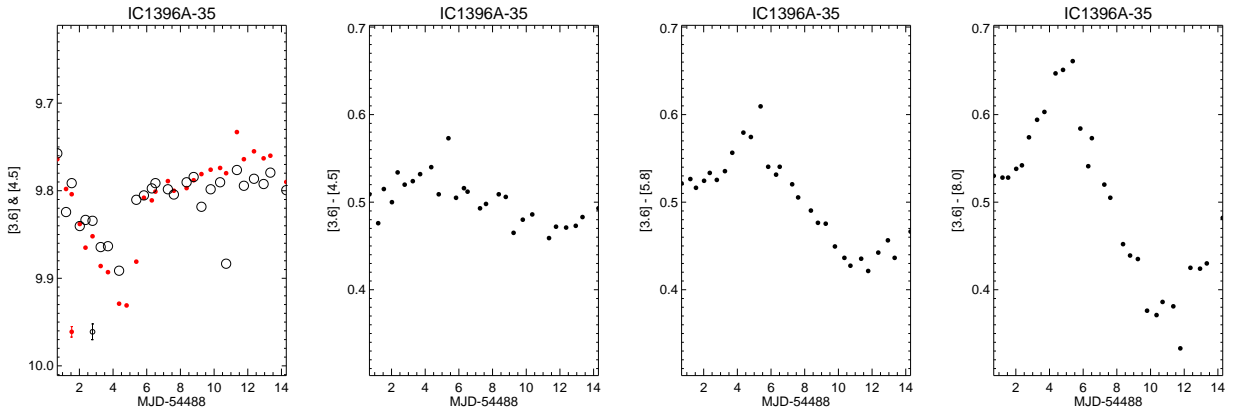


Fig. 12.— Light curves for IC1396A-35. Magnitude change with time in the rightmost diagram and changes of colors with time in the remaining diagrams. The star presents a decrease in brightness at the beginning of the observation, probably due to some obscuration process, and 4 days later the light curve becomes constant. The peak-to-peak amplitude in the color variation increases from 0.05 mag in [3.6]-[4.5] to 0.3 mag in [3.6]-[8.0].

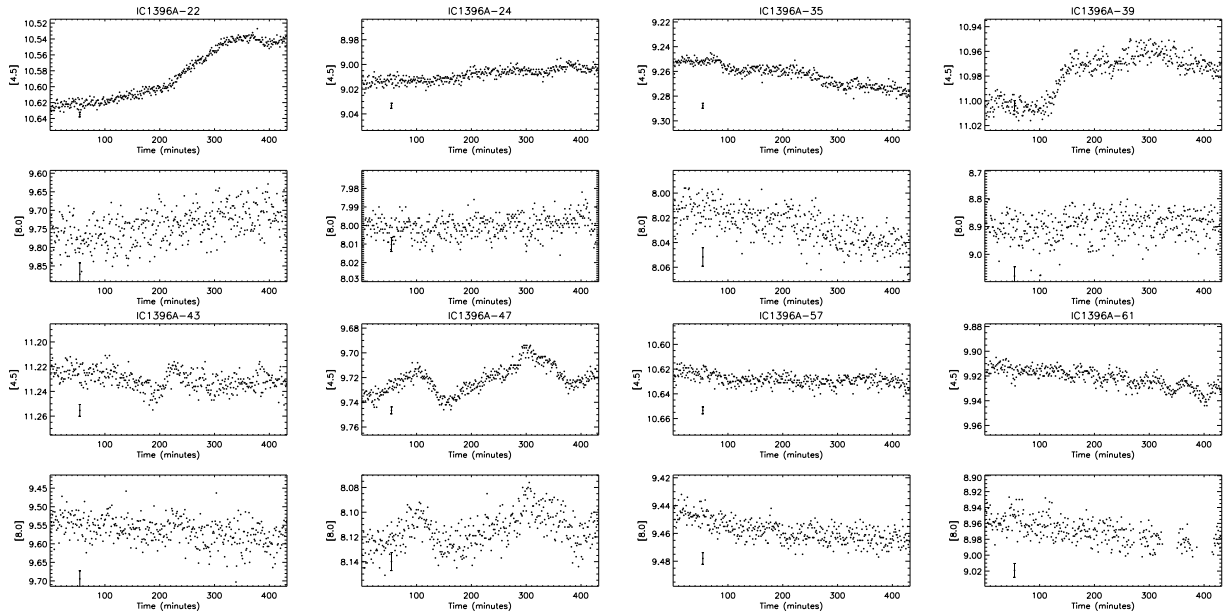


Fig. 13.— Light curves for the eight IC 1393A short term variable YSOs. The top and bottom panels show Ch. 2 and Ch. 4 time series, respectively. The rms uncertainty of a single point is represented in the lower left corner of each panel. Note the different scales in the y axis in the upper and lower panels.

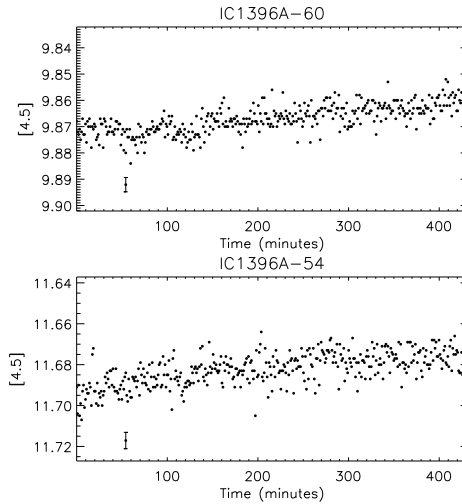


Fig. 14.— Ch. 2 light curves for the two IC 1393A YSOs which lacking the Ch. 4 light curves, do show an upward trend in their Ch. 2 light curves. The rms uncertainty of a single point is represented in the lower left corner of each panel.

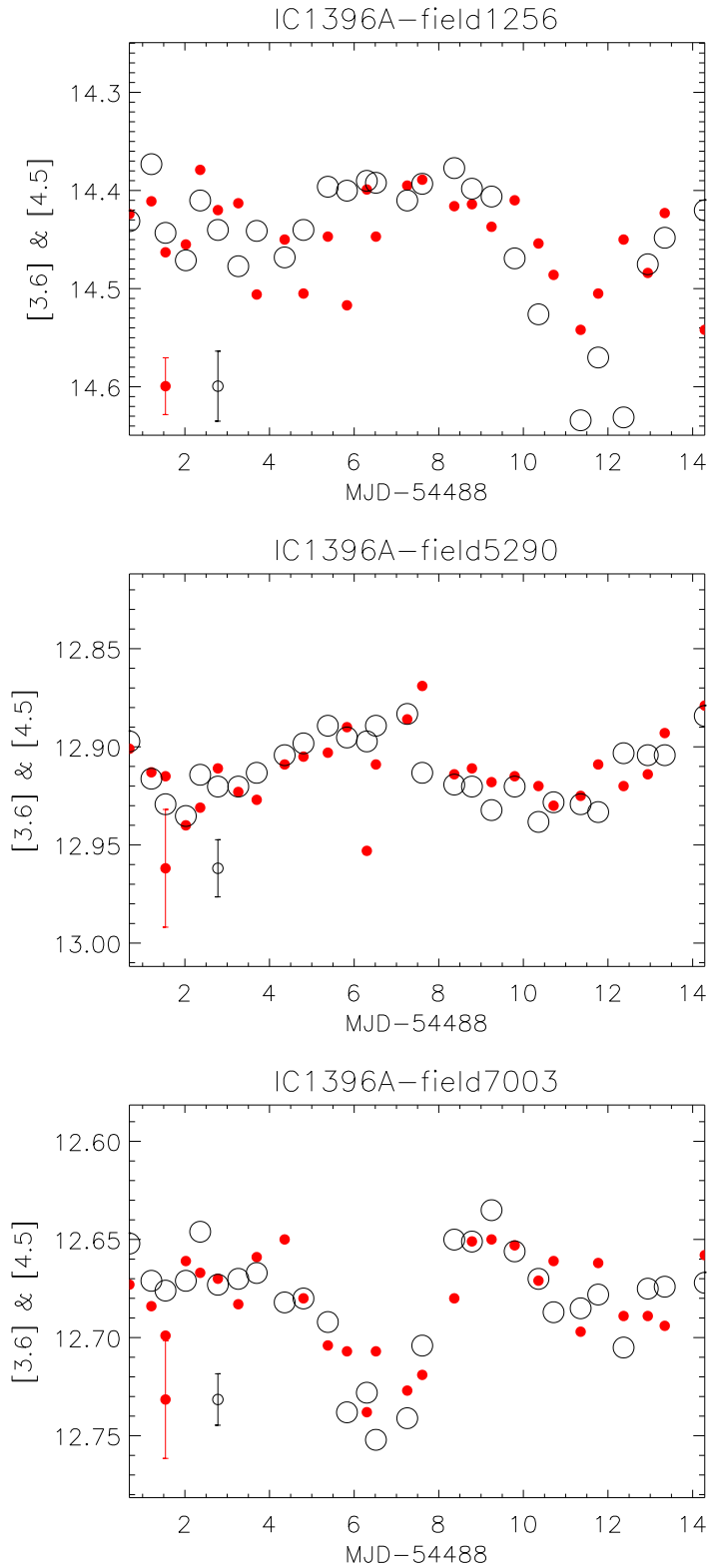


Fig. 15.— Light curves for a few variable candidate members of IC1396A from IRAC time-series observations. Red solid circles stand for the IRAC photometry at Ch. 1 (3.6  $\mu\text{m}$ ) while black open circles represent IRAC photometry at Ch. 2 (4.5  $\mu\text{m}$ ). The 4.5  $\mu\text{m}$  light curve has been shifted in the y direction so that the mean magnitude is the same as for the 3.6  $\mu\text{m}$  points. Ch. 3 & Ch. 4 light curves (not shown) show the same trends as in this plot but they are noisier.

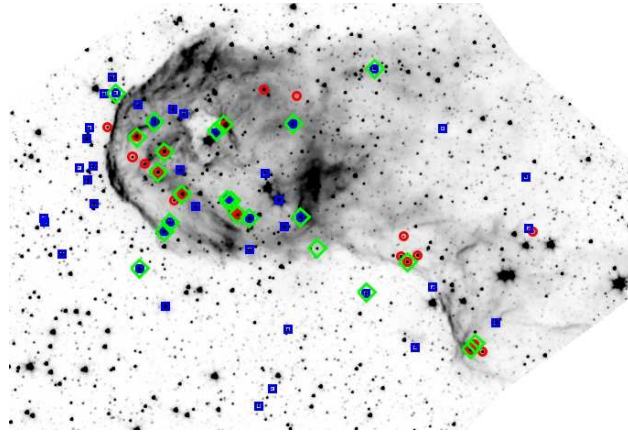


Fig. 16.— Spatial distribution of YSOs in IC1396A. Red circles represent the Class I objects, blue squares show the Class II objects, and stars with periodic-looking are plotted with green large diamonds.

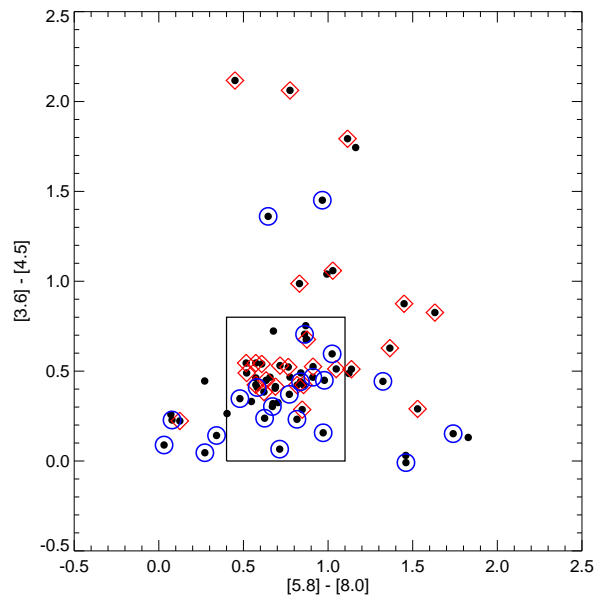


Fig. 17.— IRAC color-color diagram. Red open diamonds represent objects with variability amplitudes larger than 0.1 mag and blue circles represent constant, or almost constant YSOs.



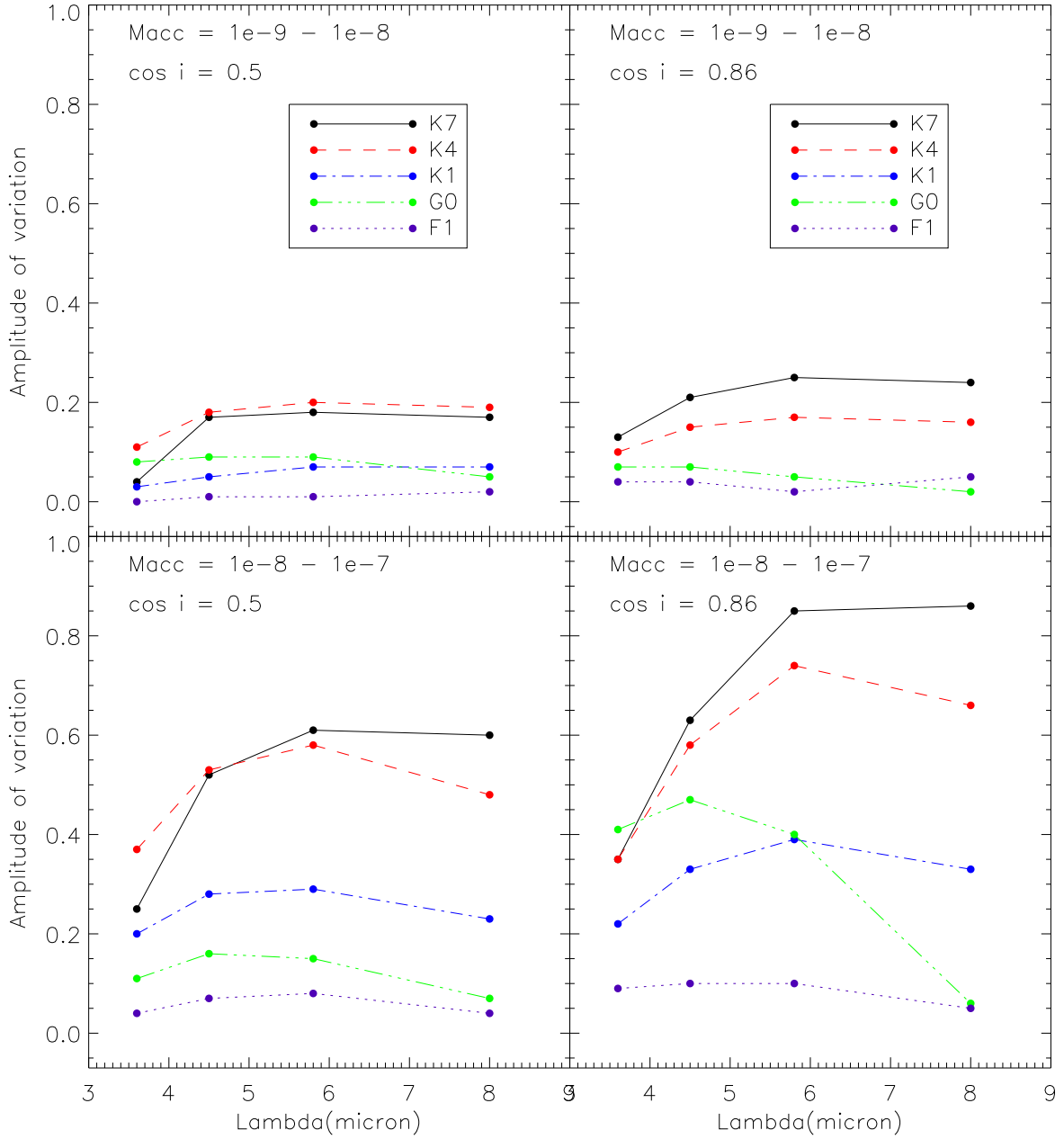


Fig. 18.— Amplitudes predicted by the disk models for a change in the mass accretion rate from  $10^{-9} M_{\odot}/\text{yr}$  up to  $10^{-8} M_{\odot}/\text{yr}$  in the upper panels and from  $10^{-8} M_{\odot}/\text{yr}$  to  $10^{-7} M_{\odot}/\text{yr}$  in the bottom ones.

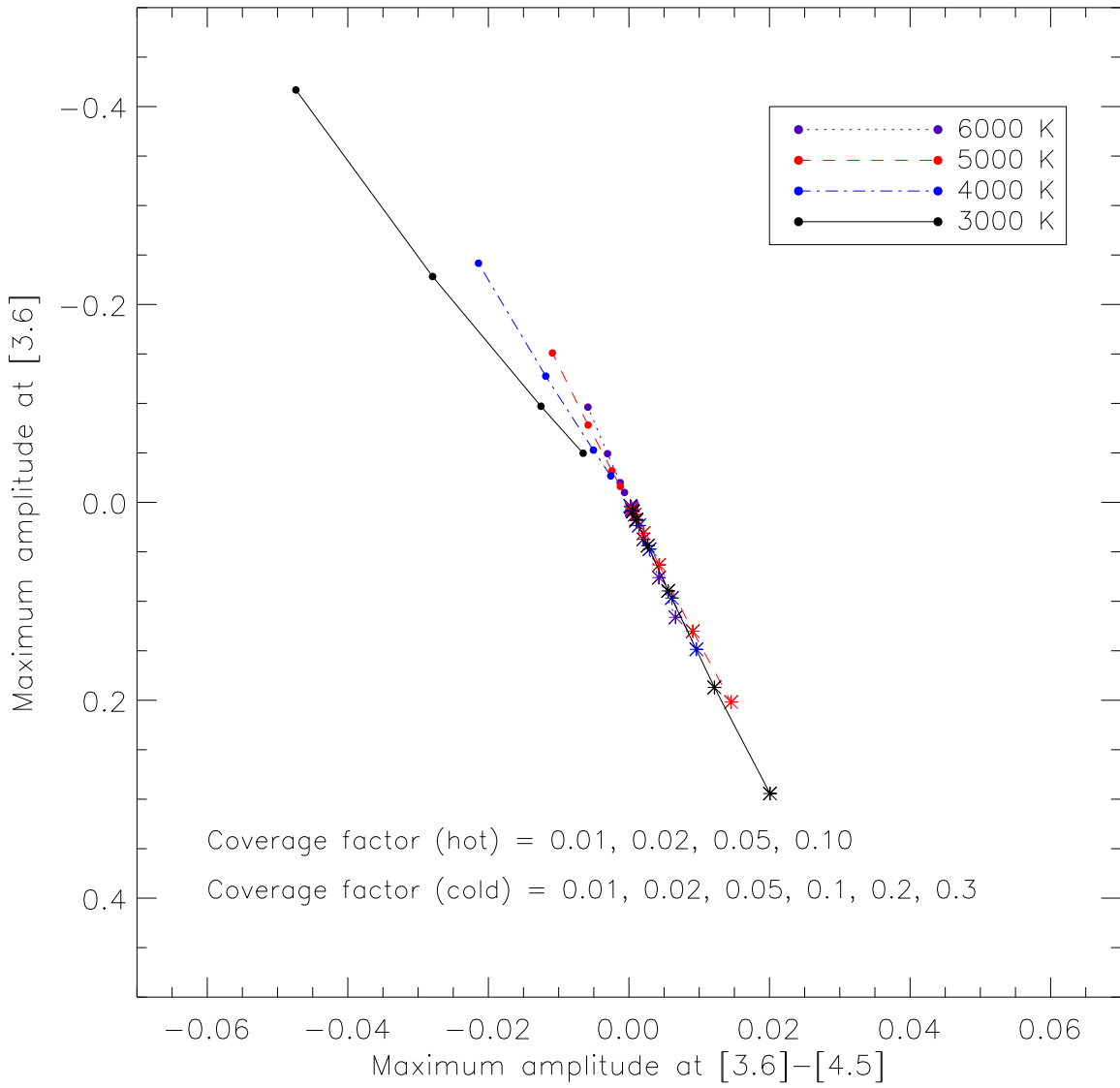


Fig. 19.— Maximum amplitudes predicted by the spot model for a set of stars with temperatures ranging from 3000 K to 6000 K. Filled circles and asterisks represent the amplitudes predicted for hot and cold spots respectively.

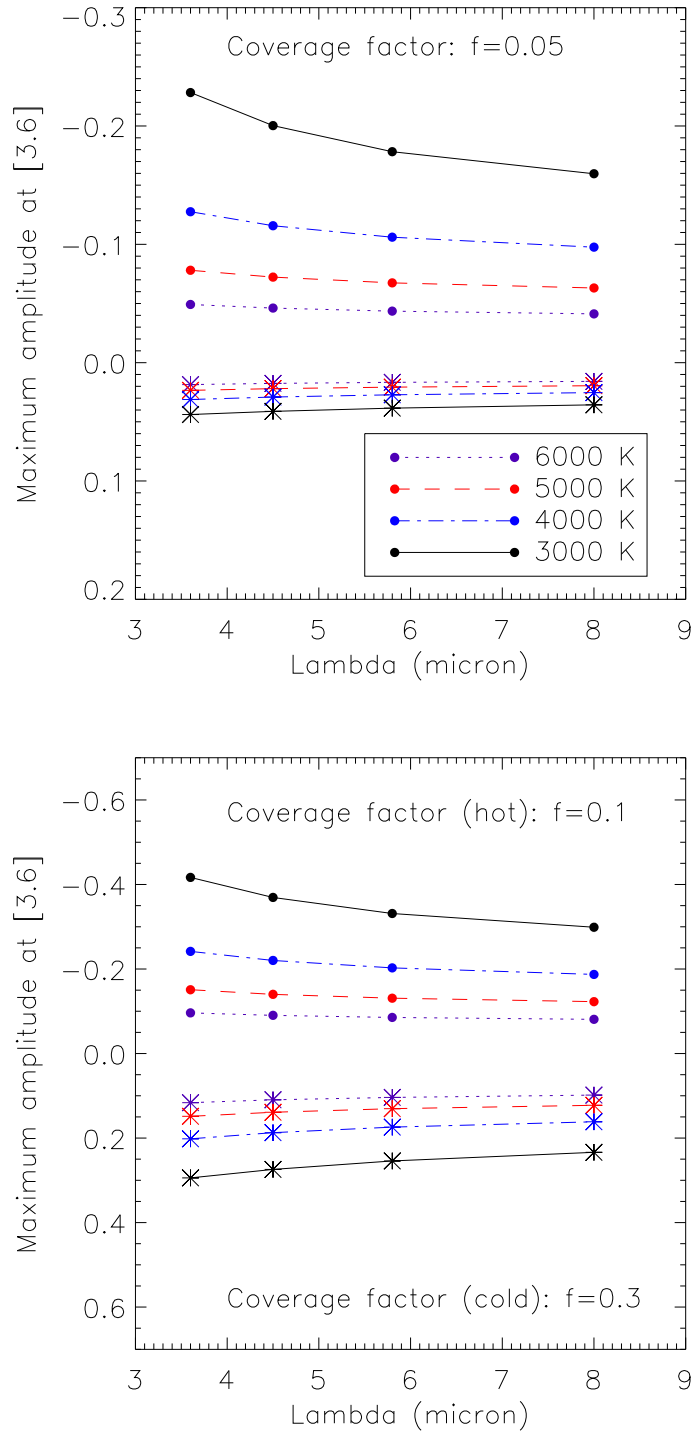


Fig. 20.— Maximum amplitudes predicted by the spot model for a set of stars with temperatures ranging from 3000 K to 6000 K. Filled circles and asterisks represent the amplitudes predicted for hot and cold spots respectively. The upper panel show intermediate coverage factor while the bottom panel presents a more extreme situation with a coverage factor of 0.1 for hot spots and a coverage factor of 0.3 for cold spots.

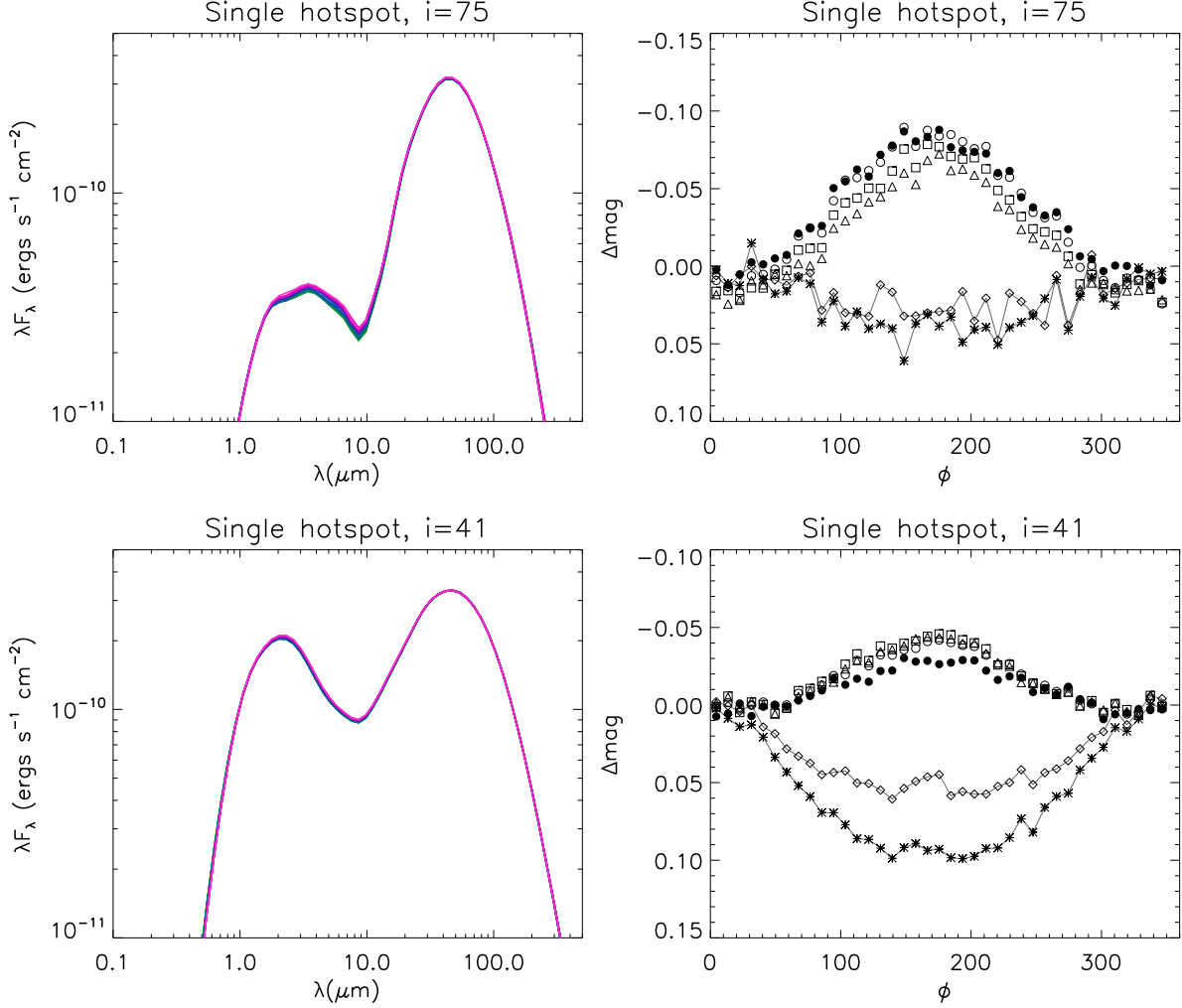


Fig. 21.— Model results for a Class I object with a hot spot on the photosphere, at a latitude of  $45^\circ$ . The different color SEDs (left) correspond to different phase angles; and the light curves (right) show one full rotation period at various wavebands (asterisk: V-band, diamond: R-band, triangle: [3.6], box: [4.5], open circle: [5.8], and filled circle: [8.0]). The V- and R-band lightcurves are connected by lines to distinguish them from the IR lightcurves. Phase 0 corresponds to the stellar hot spot facing the observer. At phase=180 degrees, the hot spot is obscured and the heated far wall faces the observer. Positive  $\Delta\text{mag}$  corresponds to fainter fluxes. The visible light curves are noisier and washed out due to extinction and scattering from the envelope. The result are periodic colorless IR variations with amplitudes similar to those that we observe at IRAC bands, and with the brightest optical phase corresponding to the faintest IRAC phase. At more pole-on viewing angles (bottom panels), the visible light curves show more variation, and the IR lightcurves show less. This is because the stellar hot spot, located at 45 degrees latitude, shows more pronounced variation with rotation, whereas the flux from the inner disk shows less phase dependence with more pole-on viewing angle.

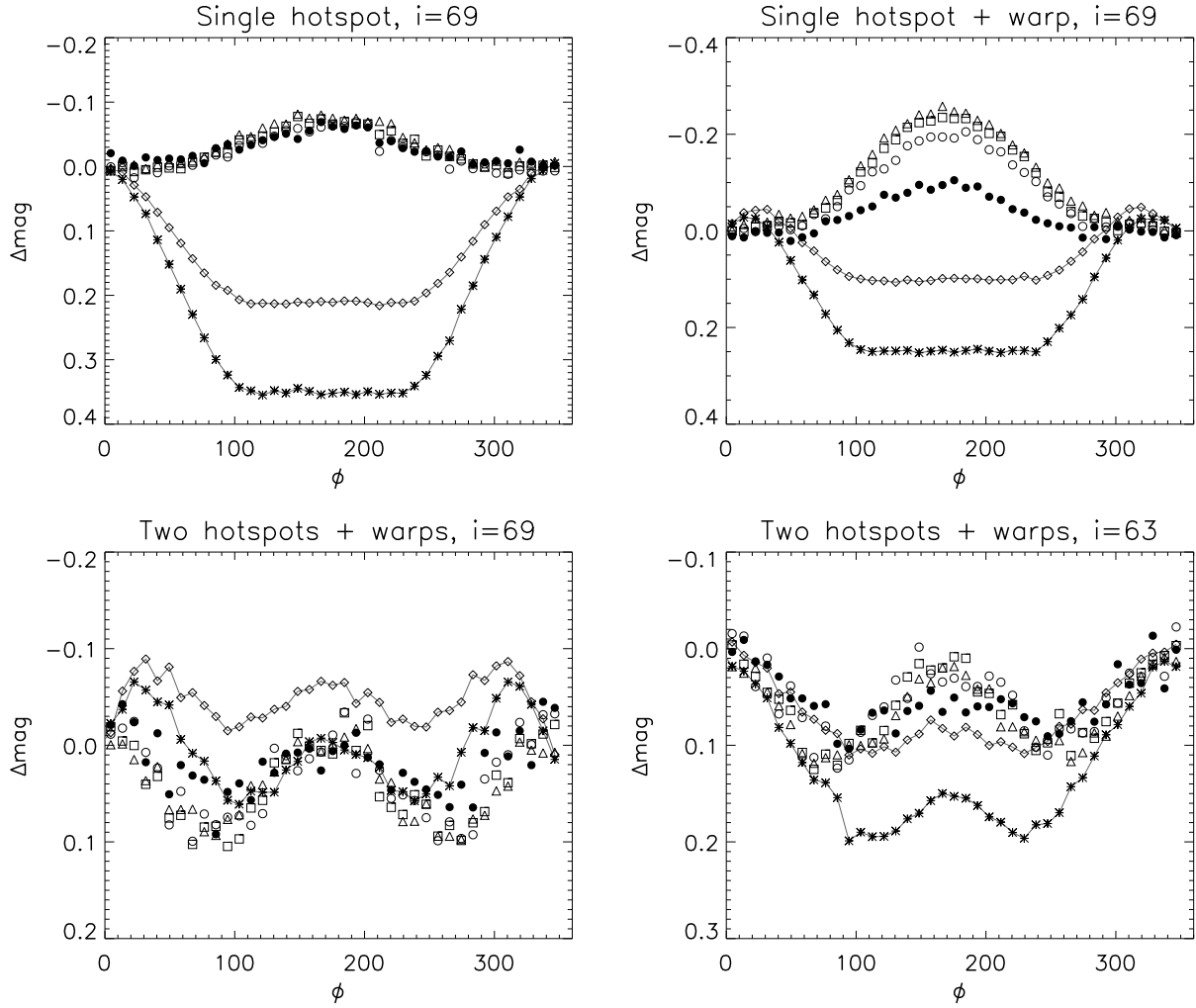


Fig. 22.— Hot spot model results for a Class II source. The top left model has the same stellar, disk, and hotspot parameters as Figure 21, but no envelope. The visible light curves show more variation without the envelope. The top right model adds a warp in the disk, raising the disk height 25% at the longitude of the hotspot. This decreases the visible variation and increases the IR. The bottom two models have 2 spots located  $180^\circ$  apart in longitude and disk warps at the spot longitudes. The visible light curves vary more with inclination (bottom left and bottom right). The symbols are as in previous Figure.

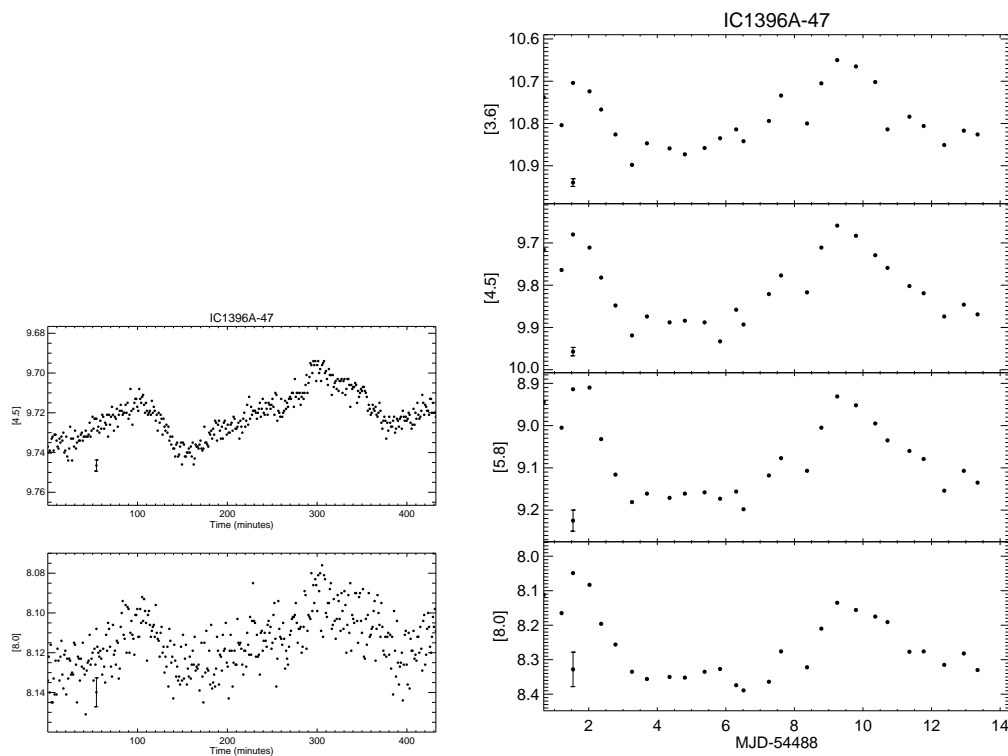


Fig. 23.— **a)** Light curves of IC1396A-47 (object  $\zeta$ ) showing the 3.5 hours period variation from the 7 hour staring-mode IRAC observation. The top and bottom panels show Ch. 2 and Ch. 4 time series, respectively. **b)** Light curves of the same object from IRAC mapping observations showing the  $\sim 9$  days period variation in the four IRAC bandpasses.